

Point Defects in LiNbO₃

Summary. In a survey of recent publications, the relationship between photorefraction and defect structure is outlined. We start with a description of the situation in undoped lithium niobate at moderate temperature. Changes in spectral characteristics (optical absorption, EPR) caused by reduction treatments and their interpretation using the polaron model are discussed then. The characteristics are used as tests for Nb antisites, i.e., Nb on an Li site. Hydrogen is the first candidate to form an extrinsic defect influencing via the protonic conductivity the charge transport (photorefraction, thermal fixation).

In a next step the photorefractive impurities like the transition metals Fe, Cu, Mn, and Ni are discussed in detail, with special emphasis on iron. Some interesting features of Cr and lanthanide ions supplement this topic. Optical-damage-resistant impurities (Mg, Zn, Sc, In, Hf, and Zr) are antagonists of Nb antisites and strongly reduce the photorefraction, when doping above certain threshold concentrations. These dopants increase the phase transition temperature, the density and shift the bandedge absorption towards the UV. Many properties differ below and above the threshold concentrations, which strongly depend on the crystal composition. Near stoichiometric samples have thresholds at much lower concentrations than congruent ones. A table with energies of the OH stretch mode in lithium niobate closes this chapter.

The origin of the *intrinsic* (structure) and *extrinsic* (impurity) point defects in the LiNbO₃ crystal lattice is a subject of several monographs and reviews listed in Sect. 1. Later, we summarize briefly the fundamentals formulated in this literature, dwelling more specifically on recent publications. The discussion is carried out mainly in view of the relationship between photorefraction and defect structure. This is the reason for choosing certain defects in the subsequent sections. We start with a presentation of the ionic radii r_i of the elements discussed in this chapter, see Table 2.1. We use the system proposed by Shannon and Prewitt [40], so the presented data correspond to the coordination number 6 in accordance with the LiNbO₃ crystal structure. As known, several definitions of r_i exist, the discrepancy between them being within 15–20 pm.

Table 2.1. Ionic radii

Ion	Li ⁺	Nb ⁵⁺	Fe ²⁺	Fe ³⁺	Cr ³⁺	Mg ²⁺	Zn ²⁺	
<i>r</i> _i (pm)	76	64	78	64.5	61.5	72	74	
Ion	Sc ³⁺	In ³⁺	Hf ⁴⁺	Zr ⁴⁺	Nd ³⁺	Er ³⁺	Na ⁺	K ⁺
<i>r</i> _i (pm)	74.5	81	71	79	98	89	102	138

2.1 Intrinsic Defect Structure of LiNbO₃

As shown in Chap. 1, LiNbO₃ belongs to the pseudoilmenite structure formed by distorted niobium–oxygen octahedra. Chains of the distorted oxygen octahedra having common faces, are aligned along the polar axis c . In the nonpolar centrosymmetric phase at $T > T_c$ the Li⁺ ions are localized within the oxygen planes, whereas the Nb⁵⁺ ions are in the center of the oxygen octahedra (between the oxygen planes). In the ferroelectric phase at $T < T_c$, the Li⁺ ions are shifted with respect to the oxygen plane by 44 pm, and the Nb⁵⁺ ions by 26–27 pm with respect to the center of the octahedron. As a result, in the polar phase structure the octahedral interstitials are one-third filled by Li ions, one-third by Nb ions and one-third are empty, see Fig. 2.1. The alternation of cation sites may be schematically depicted as a chain $\cdots\text{Li-Nb}-\square\cdots\text{Li-Nb}-\square\cdots$, where \square denotes the *empty* octahedron (referred sometimes to as *vacancy*). The Li octahedron is larger, than the Nb one, because the distances between a Li ion and the closest oxygen ions are 206.8 and 211.2 pm, whereas those for an Nb ion are 188.9 and 211.2 pm, respectively [41]. A larger size of the Li octahedron may qualitatively explain a predominant incorporation of impurity ions onto Li sites as discussed later. As seen from the phase diagram (Fig. 1.2), the LiNbO₃ (methaniobate)-structure is stable within Li₂O concentrations from 47 to 50 mol.%. The congruently melting (Li-deficient) composition corresponds to the oxide concentrations 48.45 mol.% Li₂O and 51.55 mol.% Nb₂O₅ with the ratio $[\text{Li}]/[\text{Nb}] = 0.94$. Correspondingly, the congruent LiNbO₃ (denoted often as CLN) contains about 6% empty Li sites in the lattice. There is a long story of growing defect free stoichiometric LiNbO₃ (SLN), which has been briefly discussed in Chap. 1. However, in spite of the development of new growth methods and attempts of practical applications of SLN, the commercial CLN exhibit the best optical quality among all compositions of LiNbO₃. Now, we only mention that even for ratios $[\text{Li}_2\text{O}]/[\text{Nb}_2\text{O}_5] > 1$ in the melt, the crystal is Li-deficient to some extent anyhow.

At the earliest stages of the discussions of the CLN defect structure, it was reasonable to assume that the most probable defect is the oxygen vacancy, which is characteristic for all oxides. However, structure measurements [41–44] in agreement with model calculations [45] have shown a low probability for the existence of oxygen vacancies in *as-grown* crystals. Therefore LiNbO₃ is to some extent a unique oxide containing no oxygen vacancies. Further experimental studies have shown that with decreasing Li₂O content, i.e., increasing

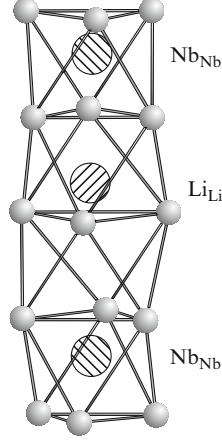


Fig. 2.1. The ideal lithium niobate with the chain $\cdots\text{Li-Nb-}\square\cdots\text{Li-Nb-}\square\cdots$, where \square denotes the *empty* octahedron

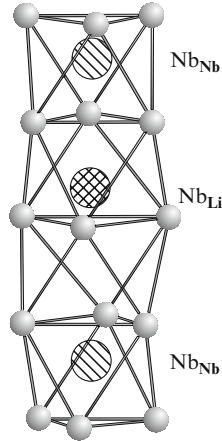
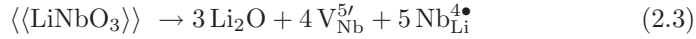


Fig. 2.2. Lithium niobate with an antisite niobium, i.e., Nb on an Li site

concentration of V_{Li} , the density of LiNbO_3 increases [46]. To overcome this paradox, some authors assumed that Nb ions incorporate partially on the Li sites [46, 47]. This is very probable, because an Nb^{5+} ion has a smaller ion radius than Li^+ (64 and 76 pm, respectively, in the sixfold coordination [40]). Therefore, the Li-deficient crystal may be formally regarded as one with a Nb surplus, or, in other words, a decreasing Li content is accompanied by an increasing content of the heavier Nb.

The existence of such a stacking fault, Nb on an Li site, (*Nb antisite*, Fig. 2.2) was repeatedly proved by structure studies [41–44], which formed the basis for defect models in LiNbO_3 .

The shortage of Li during the growth may be described by several possible processes of Li₂O outdiffusion [48]:

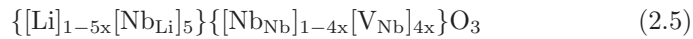


(Note that according to the Kroeger–Vink notation [49], the prime and the bullet, respectively, represent the positive and negative charge states of a defect with respect to the host; however, many authors when writing the compensation equations use the plus sign and the minus sign instead of a prime and bullet.) As mentioned earlier, the formation of oxygen vacancies is energetically unfavorable, so the compensation of the available V_{Li}' by $V_{\text{O}}^{2\bullet}$ via Reaction 2.1 should be omitted. The compensation within the cation sublattice should occur via Reaction 2.2 or 2.3.

The latter may be modified in view of the compensation of Nb_{Li} by V_{Nb} and presented in the form



The calculated energies of the defect formation via mechanisms (2.2), (2.3), or (2.4) are 4.56, 15.17, and 10.67 eV, respectively [48]. Therefore, the most energetically favorable one is mechanism (2.2), thus the compensation of Nb antisites by Li vacancies. However, this mechanism was in contradiction with the results of the pioneering work of Abrahams and Marsh [41], according to which Nb ions occupy 4.9% of the Li sites in the lattice, i.e., the *empty* Li sites are mostly populated by Nb. This gave rise to a stronger appropriateness of mechanism (2.4) for conclusions drawn from their experiments [41]. To substantiate mechanism (2.4), i.e., a compensation of $\text{Nb}_{\text{Li}}^{4\bullet}$ by Nb vacancies, despite its lower energetic benefit, Smyth [50] proposed to regard the stacking fault ($\text{Nb}_{\text{Li}}^{4\bullet} - V_{\text{Nb}}^{5'}$) as an ilmenite-type point defect (with the cation sequence $\cdots\text{AB}-\text{BA}-\text{AB}\cdots$) within the pseudo-ilmenite host, characterized by the cation sequence $\cdots\text{AB}-\text{AB}-\text{AB}\cdots$. The lattice energy calculated per unit cell of this ilmenite-type is only 0.1 eV higher than the corresponding energy for perfect LiNbO₃. These calculations supported the so-called *Nb site vacancy model* of compensation, see (2.4) and [47, 48]. The formula for congruent (Li-deficient) LiNbO₃ in this model may be described by



(the groups in the braces correspond to the population of the Li and Nb sites).

However, further structure results led to different conclusions. According to precise data of X-ray and neutron diffraction [42] only 1% of the Li sites are occupied by Nb, whereas about 4% of the Li sites are empty (Li vacancies). This existence of a high concentration of Li vacancies in congruent LiNbO₃ was confirmed by other structure reports [43, 44] and NMR studies [51]. These data

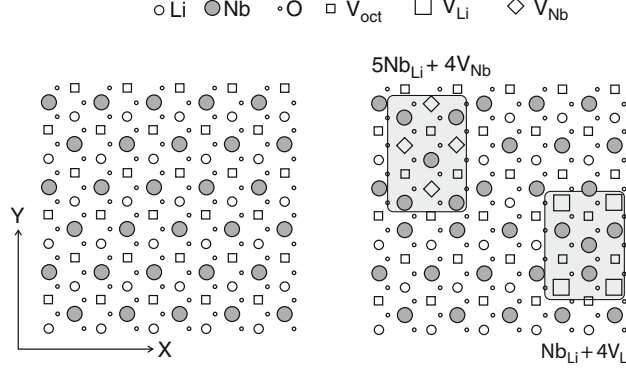


Fig. 2.3. The ideal lithium niobate structure in a projection onto the (001) plane (*left*) and the intrinsic defect Nb_{Li} with two alternatives of its compensation by Li or Nb vacancies (*right*)

supported the *Li site vacancy model*, see Reaction 2.2 and [42, 46] in which an Nb antisite is compensated by four V_{Li}, for an illustration see Fig. 2.3. In this model a congruent LiNbO₃ is described as

$$\{[\text{Li}]_{1-5x}[\text{Nb}_{\text{Li}}]_x[\text{V}_{\text{Li}}]_{4x}\}[\text{Nb}_{\text{Nb}}]\text{O}_3 \quad (2.6)$$

(here the group in the braces corresponds to the population of the Li sites).

Nowadays, the Li site vacancy model (2.6) is commonly accepted as valid and considerations of all defect reconstructions in LiNbO₃ are discussed in its framework. Nevertheless, Wilkinson et al. [43] suggested that the degree of filling the Li sites by Nb ions is accidental and depends, for example, on the growth conditions, so one may expect in as-grown Li-deficient crystals the coexistence of all three cation stacking faults Nb_{Li}, V_{Li}, and V_{Nb}.

The defect scenario discussed in this section characterizes the LiNbO₃ structure at moderate temperatures and cannot be applied to high temperatures. For example, neutron diffraction studies led to the conclusion that at high temperatures the Li position is split, so at 600 K about 9% Li atoms are missing on the regular site, being distributed between Li and vacant positions, i.e., the empty octahedron [52, 53]; this fraction increases with rising temperature. A synchrotron X-ray diffraction analysis of stoichiometric LiNbO₃ evidenced a small fraction of Li atoms on vacant sites even at room temperature [54]. It should be noted that the properties of the relative crystal LiTaO₃ is very often discussed in terms of identical structure defects Ta_{Li} and missing oxygen vacancies. Actually, the structure and optical properties of LiNbO₃ and LiTaO₃ are very similar. However, so far there is no direct proof of the existence of such stacking faults in LiTaO₃, so considerations based on this defect model are speculative in contrast to LiNbO₃. Summarizing this section, we emphasize once again that the cornerstone of the LiNbO₃ defect structure model is the existence of Nb_{Li} defects and missing oxygen vacancies,

established by structure investigations. The discussion of many properties of these crystals is based on this model, as will be shown later.

2.2 Point Defects Induced in LiNbO₃ by a Reduction Treatment and the Polaron Model

In this section, we start with a description of the spectral characteristics of LiNbO₃ after a chemical reduction. The scope of these experimental data in combination with the intrinsic defect structure outlined in the earlier section are the foundation of the currently accepted polaron model in LiNbO₃, for references see for example [55–58]. This model was initially developed and applied to reduced crystals. Later it was extended to the interpretation of the short-living electronic states arising in LiNbO₃ under intensive photoexcitation. At present short-living excited states in LiNbO₃ and related crystals are often discussed in terms of the small polaron model, sometimes rather speculatively. Let us follow the historical development of the polaron concept in LiNbO₃. Recall that the small bound polaron state is caused by a coupling of a photoinduced electron with the host phonons; the formed local polarization (or deformation) of the host serves as a potential well for the electron producing it. So, polarons are formed due to the Coulomb interaction and phonon coupling of the photoexcited charge carriers with the host ions. One should distinguish between large and small polarons. The former means that the disturbed host region exceeds significantly the lattice constant. In the latter case, the electron coupling with the host is higher, due to which the polaron radius is within the single lattice site. The transport of large polarons may be regarded as a band movement of a free electron with an effective mass, whereas a movement of small polarons occurs by hopping. Both large and small polarons may be related to electrons and holes. The polaron formation is possible if the polaron energy exceeds the electron bandwidth. Provided that the host contains charged defects, the polaron energy is decreased and polarons are localized at defect sites. This is the case of bound small polarons, unlike nonlocalized free polarons in a defect-free lattice. The transport of bound polarons as well as of free polarons occurs via hopping. The essentials, one may find in several reports [59–62]. With respect to LiNbO₃ the polaron concept was first applied at an early stage of studies of the photovoltaic effect and photorefractive effect to account for the origin of a broad absorption band within 1.5–3 eV induced in LiNbO₃ by X-ray irradiation or two-photon excitation at low temperatures [63–65]. The appearance of this band was accompanied by a rise of the EPR signal with a g -value characteristic for trapped holes ($2.002 < g < 2.047$). On this basis the induced center was identified as a capture of a photoexcited hole by one of the equivalent O²⁻ ions surrounding a cation defect, or, in other words as an O⁻ trapped hole, i.e., a small hole polaron.

The bound hole polaron exhibits a broad band in the visible with a peak at about 500 nm [65]. A coexistence of several bands attributed to different

centers in this spectral range (the hole polaron O^- , Fe^{2+} and the bipolaron discussed later) extremely hinders the interpretation. According to [66], the optical absorption of O^- is due to a hopping of a hole between equivalent adjacent O^{2-} ions surrounding a cation fault, in the case of LiNbO₃ an Li vacancy, thus binding the hole polaron to a single Li vacancy

In addition to a broad band in the visible, Arizmendi et al. [67] detected in the low temperature X-ray-induced spectral bands at 3.2 and 1.6 eV, characteristic for all LiNbO₃ crystals independent of the composition. Simultaneously, X-ray irradiation and two-photon excitation induced in LiNbO₃ a characteristic 10-line EPR spectrum, see Fig. 2.4 and [63], testifying the existence of an axial center with $g_{\perp} = 1.72$ and $g_{\parallel} = 1.9$. This center was interpreted as an electron self-trapped by the Nb_{Li}^{5+} ion (a small polaron Nb_{Li}^{4+})

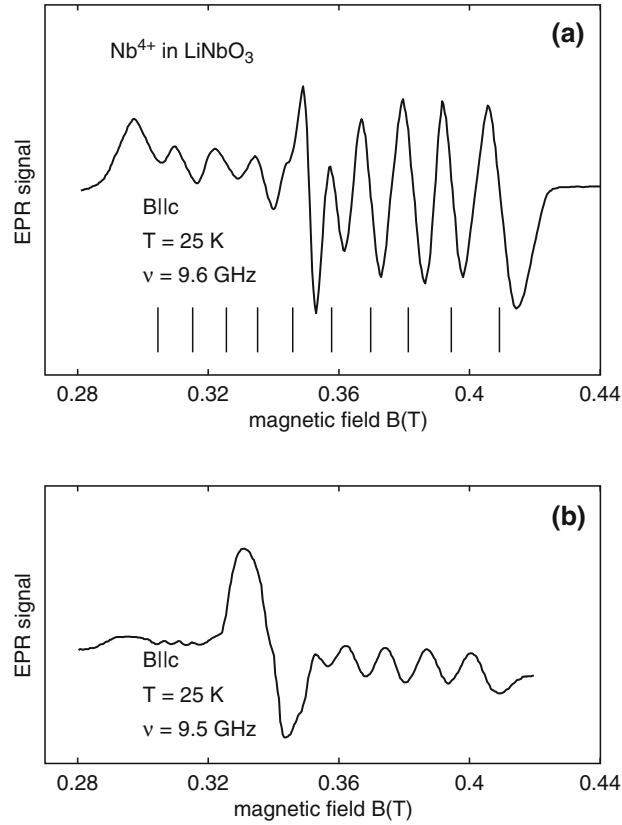


Fig. 2.4. EPR of Nb^{4+} in congruent LiNbO₃. In (a) the spectrum of a reduced and illuminated sample including the expected 10-line hyperfine structure of ^{93}Nb is shown. The additional strong line is due to Ti^{3+} . In (b) the spectrum after X-ray irradiation at low temperature is shown, the wide absorption close to 0.34 T belongs to O^- , data taken from [55]

responsible for the band 1.6 eV observed by Arizmendi et al. [67]. This conclusion formed a base for the further development of the polaron model as applied to the trapping phenomena in LiNbO₃.

We now switch to the chemical reduction of LiNbO₃. This process is performed by annealing a crystal either in vacuum, in a hydrogen atmosphere, or in an inert gas. The desirable annealing temperature is within 400–600°C, because as mentioned in the earlier section, at higher temperatures the cation sublattice seems to be disturbed [52, 53] and the reduction process is accompanied by the formation of oxygen vacancies [69]. To avoid an Li loss during reduction it is better to embed the crystal into an Li salt (e.g., Li carbonate). The spectrum of a reduced congruent (Li-deficient) undoped LiNbO₃ crystal reveals a stable broad dichroic absorption band with a maximum at about 2.5 eV, see Fig. 2.5. The origin of this band was the subject of a long discussion, one may find an appropriate bibliography in [70]. At those times the most likely was to relate it to a formation of oxygen vacancies according to (2.7)



whose thermal ionization (2.8)



would provide an increased conductivity in reduced LiNbO₃. However, a structure proof of missing oxygen vacancies in LiNbO₃ undermined this mechanism. There are additional experimental arguments disproving the role of oxygen vacancies in the reduction process. First, after a weak reduction oxygen sites

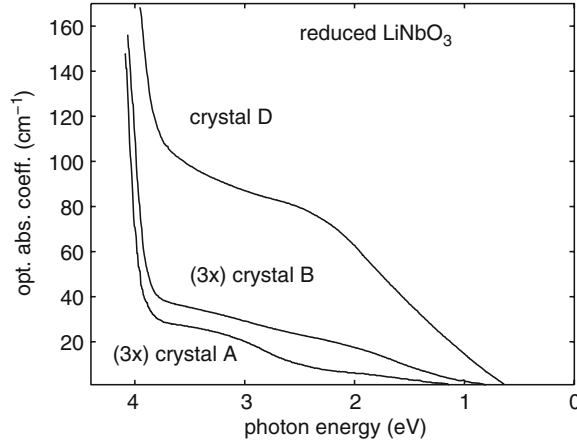
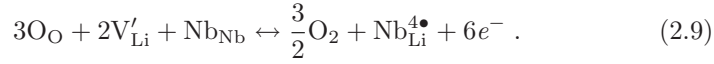


Fig. 2.5. Optical absorption of three reduced crystals with different [Li]/[Nb] ratios (crystal D with [Li]/[Nb]_{crystal} < 0.92, crystal B with [Li]/[Nb]_{crystal} = 0.976, and crystal A with [Li]/[Nb]_{crystal} = 1, respectively). The reduction temperature is 900°C in all cases, redrawn from [68]

remain almost fully occupied. Second, the density of the crystals increases after reduction, which is incompatible with the creation of V_O [71]. Finally, the intensity of this band strongly decreases in Li-enriched crystals (Fig. 2.5), which may scarcely be interpreted in terms of a formation of oxygen vacancies [68]. We should note that the role of the anion sublattice in the reduction of LiNbO₃ has not been completely ruled out yet. Although at present, the spectroscopic properties of reduced LiNbO₃ are discussed dominantly in terms of the polaron model discussed later, there is a scope of data not lying within its framework. These data will be listed later.

After finding in CLN an Nb_{Li} structure defect an alternative model (2.9) for the reduction process was proposed [48, 71]



According to this model a loss of oxygen from an LiNbO₃ surface molecule, is accompanied by an incorporation of the left Nb⁵⁺ ion onto the empty Li site and ultimately to a total redistribution of V_{Li} and Nb_{Li} ; the electrons are trapped by Nb. The oxygen leaves the crystal surface, so no oxygen vacancies appear at the end; the released electrons are captured by traps. The reduced crystal is diamagnetic, so the absorption band itself cannot be assigned to the electron capture by Nb_{Li} forming a paramagnetic Nb_{Li}⁴⁺. As was assumed by Schirmer et al. [72] and supported by model calculations [48, 70] the electrons are captured by the pre-existing or newly formed neighboring complexes Nb_{Nb}–Nb_{Li} to form a diamagnetic bipolaron, the stable bonded electron pair (Nb_{Nb}–Nb_{Li})²⁻. The formation of a bipolaron is energetically favorable [45, 48] and qualitatively means a self-stabilization of an electron pair. In the framework of this model, the broad band at 2.5 eV (Fig. 2.5) is attributed to the transfer of one of the paired electrons from the bipolaron and further capturing by an isolated Nb_{Li}, or, in other words to a dissociation of the bipolaron. The dissociation may be performed thermally or optically.

In line with this consideration, a thermal annealing of a reduced LiNbO₃ at $T > 600^\circ\text{C}$ resulted in a reversible shift of the band to 1.6 eV [73], which was interpreted as a thermal dissociation of bipolarons and a formation of isolated small polarons. From the temperature dependence of the *turnover* between the bands of the corresponding bipolarons (2.5 eV) and polarons (1.6 eV), the bipolaron dissociation energy was determined to be of about 0.3 eV [73].

The experiments on photoinduced changes of this spectrum at low temperatures seemed to support this interpretation [74, 75]. If a reduced crystal is illuminated by blue-green light at $T \leq 80\text{ K}$, then the band at 2.5 eV is pumped over to the metastable band at 1.6 eV, see (Fig. 2.6) and [67, 74, 75]. When heating to $T > 100\text{ K}$, this new band is bleached and the initial spectrum is restored. The appearance of the band at 1.6 eV is accompanied by the rise of a characteristic 10-line EPR pattern (Fig. 2.4), which is thermally annealed simultaneously with the decay of the band at 1.6 eV with the same activation energy [70]. The photoinduced EPR pattern was identical to that

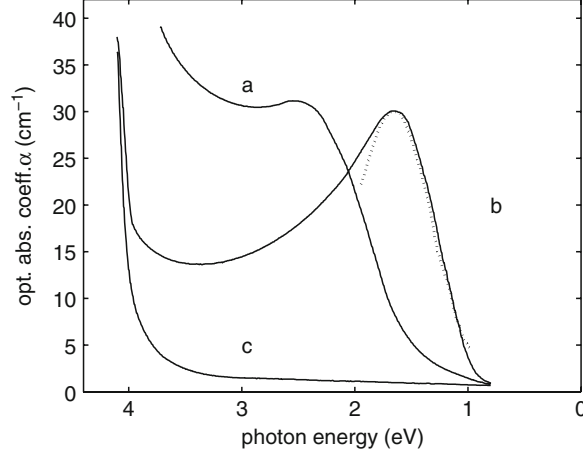


Fig. 2.6. Optical absorption α of congruent reduced LiNbO₃. (a) The bipolaron band at 2.5 eV before illumination. (b) After illumination at $T < 100$ K with the Nb_{Li}^{3•} polaron. The *dotted part* is a fit with (2.11)

observed under X-ray irradiation of LiNbO₃ at low temperatures [63], which, recall, was attributed to a formation of the small polaron Nb_{Li}⁴⁺. The scope of these data allowed to regard the reconstruction of the absorption spectrum under illumination as a proof of the optical dissociation of the bipolaron following the scheme



The polaron band at 1.6 eV is ascribed to an optical transfer of an electron from Nb_{Li}⁴⁺ to one of the surrounding Nb_{Nb} ions [55, 70]. The validity of the interpretation of the band at 1.6 eV as a Nb_{Li}⁴⁺ small polaron was supported by certain estimations. The absorption of the small bound polaron is described with an expression like [55, 58, 59]

$$\alpha(\omega) = \frac{D}{\hbar\omega} \exp\left(-\frac{(4U + \epsilon - \hbar\omega)^2}{8\hbar\omega_0}\right), \quad (2.11)$$

where $\omega = 2\pi c/\lambda$, $\hbar\omega_0$ is the phonon energy, U the polaron stabilization energy, ϵ the energy corresponding to the optical transfer of a small polaron between nonequivalent sites, and D a measure for the amplitude. The photoinduced absorption band at 1.6 eV was fitted [55] by the function (2.11) using a typical value of $\hbar\omega_0 \sim 0.1$ eV and a polaron stabilization energy $U \sim 0.3$ eV according to the estimates from the thermal dissociation of bipolarons [73]. The fitted curve (dotted in Fig. 2.6) is in agreement with the experimental absorption band. Another proof was provided by measurements of the temperature dependence of the conductivity, which found an activation energy of 0.49 eV [70]. The ratio of the optical energy of 1.6 eV to the

thermal activation energy is $\approx 4:1$, so being in a satisfactory agreement with the ratio required for the small polaron model [60, 61]. Recent experiments in reduced LiNbO₃, enlarging the spectral range of studies in the polaron states to 5 μm [57] found one more absorption band at 0.38 eV. These authors assigned it to an optical transition between Nb_{Li} and Nb_{Nb} polaron levels.

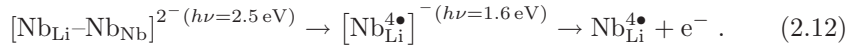
This whole consideration concerned the Li-deficient (congruent) LiNbO₃. One may see (see Fig. 2.5) an essential decrease of this band with increasing [Li], i.e., with a decrease of [Nb_{Li}]. With respect to the reduction equation (2.9) this dependence is qualitatively clear. However, no such experiments have been performed in stoichiometric crystals (totally free of Nb_{Li}), because at those times, when intensive studies of the LiNbO₃ defect structure were performed, the growth of the stoichiometric crystals had not been elaborated, yet. At the same time, Sweeney et al. [76] observed a fundamental dissimilarity of the absorption spectrum in reduced highly doped (*above-threshold*) LiNbO₃:Mg from the spectra in reduced undoped (or low-doped) crystals. After a rather hard reduction treatment in highly doped LiNbO₃:Mg no absorption band appeared in the visible area, whereas a stable broad band arose at about 0.95 eV, which was assigned in [76] to an electron captured by the trap [Mg_{Li}]⁺. For this band, some authors [77, 78] proposed another explanation, starting from the assumption that the threshold concentration corresponds to the disappearance of Nb antisites from the lattice due to their substitution by Mg ions, for details see the Sect. 2.5. So, in the framework of this substitution scheme, highly doped LiNbO₃:Mg crystals were taken as a model for an LiNbO₃ free of Nb_{Li}, and distinctive features of their spectroscopic characteristics after reduction were attributed to missing Nb antisites. The band at 0.95 eV was ascribed to a free small polaron Nb_{Nb}⁴⁺ resulting from a capture of electrons released under reduction, by a regular Nb_{Nb}⁵⁺ ion and coupling to an unknown lattice perturbation [77, 78]. In this presentation, the band at 0.95 eV characterizes an electron hopping between equivalent sites Nb_{Nb}. A low temperature illumination does not affect this absorption spectrum and induces no EPR lines, thus, in other words, no events happen which are characteristic for the congruent crystals and related to Nb antisites.

We now list the data that are inconsistent with the above explanation of the reducing process in LiNbO₃ crystals. The interpretation of the band in the visible is not unambiguous. Formerly some authors [67, 68, 79] assigned it, at least partially to a contribution from oxygen vacancies. Some authors [65, 74, 75] found the photoinduced transformations of this band at low temperatures (Fig. 2.6), attributed the observed effects to a photoexcitation of charged oxygen vacancies. The existence of V_O in LiNbO₃ may be concluded from the experiments on reducing LiNbO₃ in an inert atmosphere under external field [69] or from optical absorption spectra of Ar-implanted LiNbO₃ [80]. The detailed in situ studies of the optical absorption spectra under reduction/oxidation of congruent LiNbO₃ established a removal of oxygen, that is the formation of V_O and their contribution to the absorption band in visible, if the reduction treatment was performed at $T > 600^\circ\text{C}$.

According to the polaron model, all the spectral characteristics of reduced crystals are often used as a *test* for Nb antisites. The appearance of a band at 0.95 eV after reduction is an evidence of missing Nb_{Li}, whereas a photoinduced EPR structure arising in a reduced crystal (Fig. 2.4) combined with a red-shift of the absorption band (1.6 eV, see Fig. 2.6) produces evidence for the presence of Nb_{Li}. The main assumption underlying these tests is that a moderate reduction treatment does not affect or affects very slightly the initial concentration of Nb antisites. As shown later, in terms of these tests the defect structure in the optical-damage-resistant LiNbO₃ crystals was analyzed. At the same time, we should mention again that there is a lack of a careful study of these effects in undoped stoichiometric crystals.

According to Fig. 2.5, in near-stoichiometric crystals (NSLN for LiNbO₃ and NSLT for LiTaO₃) the absorption band in the visible may be also induced by a reduction treatment, although it is weaker than in Li-deficient ones. Its existence is supported by recent data of reduction experiments in NSLN grown by the Czochralski technique from a K₂O-supplemented melt [81] and in NSLN crystals produced by the VTE-technique [82]. No investigations of this band similar to those in the congruent crystals (the photoinduced effects, EPR measurements, etc., described earlier), have been performed in reduced near-stoichiometric ones, which could help in the interpretation of the observed optical absorption. As in stoichiometric crystals, an interpretation of this band in the framework of the polaron model is not appropriate, so it may be related either to oxygen vacancies or to unintentional admixtures. We emphasize again that the formation of oxygen vacancies is provoked by using too high temperatures for the reduction. Recently, the reduction conditions aimed to the studies of bipolarons in reduced crystals were refined in [83]. When annealing congruent LiNbO₃ samples in vacuum at $T \approx 600^\circ\text{C}$ for several hours, a stable noticeable absorption band in the visible appears and steeply grows with T (Fig. 2.7).

Experiments on the photoinduced dissociation of bipolarons by Reaction 2.10 formed a basis for an IR hologram recording in reduced LiNbO₃ in the two-color gating regime [84]. This subject will be discussed in more detail in Sect. 5.1 devoted to a nonvolatile optical readout of the photorefractive gratings, so we now restrict ourselves to an outline of the principle of this recording. The absorption band corresponding to the small polaron provides a possible photoexcitation of free electrons at 1.6 eV ($\lambda \approx 800\text{ nm}$). This can be used for recording a grating by a spatially modulated IR light of this spectral range. In this case, a two-step photoexcitation process (the bipolaron photodissociation and subsequent small polaron photoexcitation) should be involved



Actually, in accordance with this scheme in a reduced LiNbO₃ a recording grating was achieved with $\lambda = 852\text{ nm}$ (from a Ti-sapphire laser) under simultaneously pumping with spatially uniform visible light $\lambda = 488\text{ nm}$ [84,85].

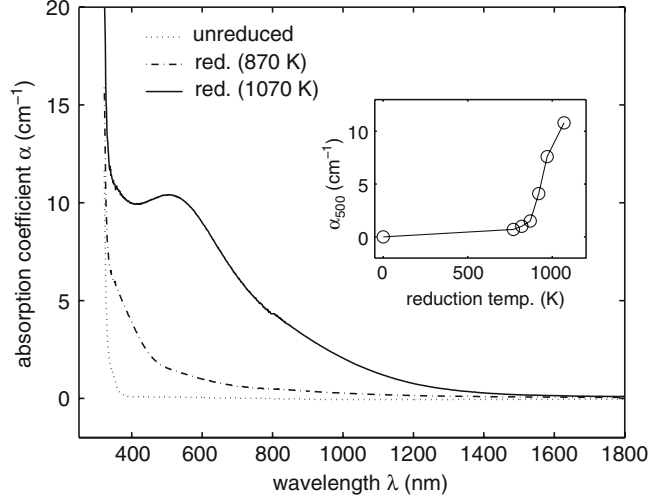


Fig. 2.7. Steady-state absorption of unreduced and reduced LiNbO₃. The absorption at $\lambda = 500$ nm as a function of the reduction temperature is shown in the inset, redrawn from [83]

This process was interpreted in terms of the two-step scheme (2.12). Thus, in reduced LiNbO₃ crystals a small polaron Nb_{Li}⁴⁺ serves as an intermediate short-living center for the IR recording. These practically interesting results stimulated wide studies of the absorption band at 1.6 eV in reduced LiNbO₃ of different composition. As mentioned earlier, in undoped LiNbO₃ this band is stable at $T < 80$ K and short-living at room temperature, i.e., about μ s in LiNbO₃:Fe [86]. It was found, that its decay time (i.e., the lifetime of the small polaron Nb_{Li}⁴⁺) very strongly depends on the crystal composition, for example, it increases up to 10–100 ms in the crystals close to the stoichiometric composition [84, 87] and even up to several seconds in Li-enriched LiNbO₃:Mg crystals [88]. Doping of LiNbO₃ with some rare earth impurities, such as Pr [89–91] or Tb [92, 93], also seems to increase this time. The dependence of the lifetime on the crystal composition might be accounted for by a kinetic compromise between the electron photoexcitation and the capturing Nb_{Li}⁴⁺ \leftrightarrow Nb_{Li}⁵⁺ + e[−]. The role of the rare earths is still a mystery.

The polaron model was further applied to the interpretation of the short-living photoexcited states in LiNbO₃. Due to the development of ultrashort optical pulses, recently a great progress was achieved in this topic since the pioneering investigations of the photoexcitation of LiNbO₃ under intensive light pulses [94, 95]. This subject will be outlined in the Sect. 5.1 devoted to the two-color holographic recording. We now dwell on the recent experiments [58, 86, 96, 97] aimed to analyze the short-living photoinduced coloration in LiNbO₃. A novelty of these experiments is their particular concentration on the formation of small polarons Nb_{Li}⁴⁺ and thus a discussion of

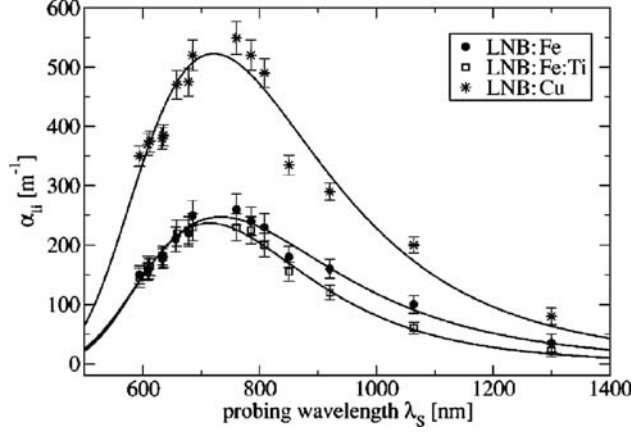


Fig. 2.8. Maximum of the light-induced absorption on the probing beam. *Solid lines* represent fits using (2.11), taken from [58]. Reprinted figure with permission from P. Herth, D. Schaniel, T. Woike, T. Granzow, M. Imlau, E. Krätzig, Physical Review B, 71, 125128 (2005). Copyright 2005 by the American Physical Society

the results in terms of the polaron model. In these works the photoinduced optical absorption $\Delta\alpha$ was studied using the pump-probe technique. This means that $\Delta\alpha$ was pumped by a short light pulse with a wavelength in the visible, i.e., $\lambda_p = 532$ nm and pulse duration in the range of nanoseconds [58, 86, 96]. An even shorter wavelength $\lambda_p = 388$ nm and pulse duration (240 fs) were recently used [97]. The probing was performed with a delayed short pulse or even CW-light at a suitable wavelength. The spectral dependencies of $\Delta\alpha(\lambda)$ obtained in several compositions (LiNbO₃:Fe, LiNbO₃:Fe:Ti, LiNbO₃:Cu), are characterized by two ranges, namely, by a broad band in the visible and a broad band in the near IR with the maximum at about 740 nm (1.67 eV), see Fig. 2.8. The former is trivial, its spectral features depend on the composition and are related to a nonequilibrium overfilling of the capture levels. The band at 740 nm does not depend on the composition, thus it is common for all LiNbO₃ crystals. As the spectral position of this band is close to the photoinduced band in reduced LiNbO₃ (Fig. 2.6), so the authors analyzed its relation to the Nb_{Li}⁴⁺ center and fitted the bandshape using the function (2.11), the fits are shown by the solid curves in Fig. 2.8. The curves in all crystals are in good agreement with the experimental data and the estimated values of the polaron stabilization energy are in the range of 0.3 eV and thus close to the value of U obtained for the photoinduced IR band in reduced crystals. Herth et al. [58] interpreted the observed photoinduced IR band as a bound small polaron Nb_{Li}⁴⁺. Spectral studies of the photoinduced absorption in the near IR led Beyer et al. [97] to the same conclusion. Their usage of ultrashort pumping pulses permitted them to resolve the formation time of this center, which is according to their estimates within 400 fs. The decay of the band

follows a single stretched exponential law $A_0 \exp[-(t/\tau)^\beta]$ with $\beta = \text{constant}$ for a given temperature and τ in the range of μs at room temperature.

The kinetics via stretched exponentials do not reply to the requirements of the two-center model [98] according to which the relaxation of a photoinduced absorption should occur by a single-exponent. Recall that the stretched exponential (referred to sometimes as the Kohlrausch law) may be regarded as a superposition of an infinity number of single-exponents, so τ characterizes a mean value of different lifetimes. To account for the observed kinetics Berben et al. [86] suggested that the relaxation occurs via hopping of charge carriers over shallow levels up to a capture by a deep trap. The probability P of this process depends on the distance r between sites ($P \propto \exp(-r)$), in other words in the discussed case on the concentration of Nb_{Li} . The numerical simulations gave a satisfactory agreement with the experimentally observed decay kinetics.

Probing $\Delta\alpha(\lambda)$ in the spectral range 1,300–1,500 nm detected no evidences for the presence of free small polarons [97]. The scope of these data is of fundamental importance for the charge transport scheme in LiNbO₃, because, as will be shown later, the defect Nb_{Li} is regarded as the most probable shallow (secondary) electron trap, whose participation in the charge transport scheme can explain the observed peculiarities of the photoconductivity, the photovoltaic currents, the photorefractive and others, especially under an intensive irradiation. Therefore, the data presented [58, 86, 96, 97] independently of their interpretation evidently support the assumption that Nb_{Li} acts as a shallow electron trap.

Recently, an interest to the formation of photoexcited bound hole polarons O^- in LiNbO₃, which was formerly attracted for interpretation of the broad absorption band in the visible resulted from X-ray irradiation or the two-photon excitation at low temperatures [63, 64] (for a bibliography on bound hole polarons in oxides see the recent review of Schirmer [66]) was resumed. A similar band with weakly pronounced maxima at about 500 and 400 nm was repeatedly reported in LiNbO₃ after X-, γ -, UV-, and electron-irradiation, one may find some references in [58, 96]. The data on its shape and relaxation kinetics are very scattered, the characteristic times depend on the composition and irradiation conditions. As mentioned earlier, the coexistence of absorption bands attributed to various centers (Fe^{2+} -like ions, O^- , ionized oxygen vacancies, bipolarons in reduced crystals) in this spectral range extremely hampers the interpretation. When analyzing the spectra and relaxation kinetics of the band in the blue-green spectral range induced in LiNbO₃ and LiNbO₃:Fe by irradiation with 532 nm, pulse durations of the order of nanoseconds, intensities within 0.5 GW cm^{-2} , the authors of [58, 96] concluded that a contribution from hole polarons was detected. Their conclusion was expanded to the reduced LiNbO₃ [83] and a general model of the photoexcitation with account for participation of bound small polarons, bipolarons, and $\text{Fe}^{2+}/\text{Fe}^{3+}$ was proposed.

2.3 Hydrogen in the LiNbO₃ Lattice

The bibliography on OH⁻ ions in oxides on the whole one may find in a recent review [99] and on hydrogen in LiNbO₃ in the review [100]. We shortly summarize the available material. In synthetic oxides the incorporation mechanism of hydrogen is not well understood, but it is widely accepted that it enters the lattice from the ambient atmosphere during or after the growing process. Among the possible hydrogen-based defects the hydroxyl ion OH⁻ attracts the attention by its presence in a wide range of materials. In oxide crystals, hydroxyl ions occupy oxygen sites. Its surplus positive charge with respect to the lattice ([OH_O][•]) compensates some other kinds of intrinsic or extrinsic defects, allowing one to probe the defect structure by studying the spectroscopic properties of the hydroxyl ions affected by their surroundings. A relatively low concentration of OH⁻ permits to regard them as isolated diatomic molecules in the lattice. As the hydrogen impurity is much lighter than the host atoms, so it gives rise to a localized vibrational mode with a frequency much higher than the vibrational frequencies of the host. The vibrational modes of OH⁻ are studied by IR absorption spectroscopy and Raman scattering and can be interpreted in the framework of an anharmonic oscillator model. The stretch mode frequency of the hydroxyl ion in various oxide crystals is in the range between 3,200 and 3,700 cm⁻¹, the typical halfwidth of the OH⁻ band being between 5 and 50 cm⁻¹.

An absorption band in LiNbO₃ have been reported as early as 1968 and assigned to hydrogen incorporated into the crystal [101], later polarization characteristics and the fine structure were analyzed [102]. A large number of experimental studies on the OH stretch mode in LiNbO₃ (see [99, 100] and references therein) may be shortly summarized as follows. In congruent LiNbO₃, the usually observed broad IR band has a full width at half-maximum (FWHM) of about 32 cm⁻¹, whereas in LiTaO₃ the FWHM is about 50 cm⁻¹. In LiNbO₃ strongly doped with hydrogen, the band is sufficiently broadened [103]. The absorption in congruent LiNbO₃ consists of a strong peak at 3,482 cm⁻¹ (2.87 μm) and a weaker one at 3,467 cm⁻¹ (2.88 μm), see Fig. 2.9.

Raman scattering measurements in congruent LiNbO₃ crystals have shown that the local symmetry of the OH-related defect is C₁ [104]. As well as in other oxides, the band is strongly dichroic, namely the optical absorption for the ordinary light polarization (σ) significantly exceeds that for extraordinary (π) one, i.e., the hydrogen stretching vibration occurs in the plane perpendicular to the polar *c*-axis. For a given composition of LiNbO₃ the IR band does not depend on temperature from room temperature down to liquid helium, which is unlike in other ABO₃ compounds. At the same time, the shape of the IR band in LiNbO₃ and its peak position noticeably depend on the [Li]/[Nb] ratio [102, 105]. When increasing the Li content, the peak position is shifted and the band is narrowed (Fig. 2.9) owing to the disappearance of intrinsic defects, thus a more homogeneous local environment is achieved. Similar narrowing of the OH-band was found in near-stoichiometric LiTaO₃ [39, 106]. The

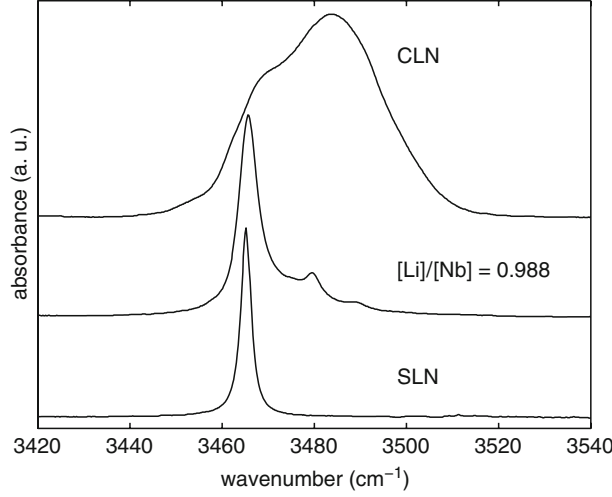


Fig. 2.9. OH absorption bands in LiNbO₃ of various composition, redrawn from [36]

dependence of the IR on other factors, such as doping with optical-damage-resistant impurities Mg, Zn, In, Sc, and even on the ferroelectric switching will be discussed in the appropriate sections.

The model proposed for the OH absorption in LiNbO₃ will be introduced in brief later [105, 107]. LiNbO₃ belongs to the pseudo-ilmenite group composed of six planar rows of oxygen atoms in a distorted close-packed hexagonal structure. The chains of distorted facet-linked oxygen octahedra are oriented along the polar *c*-axis, the oxygen planes being perpendicular. The OH stretch mode is due to protons coupling to one of the six nearest O²⁻ ions. The distortion of the oxygen octahedra results in different lengths for the available O–O bonds, i.e., in six nonequivalent sites for the hydroxyl ions. The model assumes that the longest (336 pm) O–O bonds, i.e., positions 5 and 6 in Fig. 2.10, are not occupied by OH, so the OH absorption band should be formed by four components corresponding to four different OH-bonds. Actually, a careful deconvolution of the band shapes of the OH spectra for different [Li]/[Nb] ratios gives 4 or 5 lines. From a deconvolution of the band in nearly stoichiometric LiNbO₃ the four Lorentzian components 3,465, 3,472, 3,479, and 3,488 cm⁻¹ were obtained [108], formerly only two being well resolved. So, following this model in LiNbO₃ the hydroxyl ions (or, which is the same, protons) are statistically distributed over four nonequivalent positions. The total area under the band is proportional to the whole OH concentration [109] and the intensities of the individual (deconvoluted) lines are assumed to be proportional to the amount of OH ions on the corresponding O sites [108]. As shown in [108], this distribution is not in equilibrium, because in stoichiometric LiNbO₃ at elevated temperatures the intensities of the IR lines vary very slowly on a time scale of 10 h. Particularly, the intensities of the lines 3,472 and 3,488 cm⁻¹

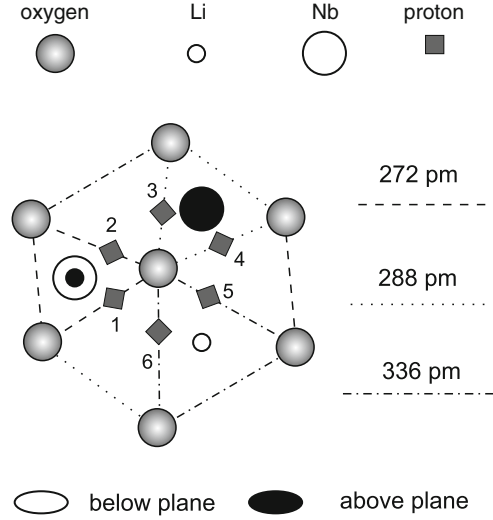


Fig. 2.10. A schematic drawing of the oxygen plane perpendicular to the c -axis, redrawn from [107]

increase at the expense of 3,465 and 3,479 cm^{-1} , the total area under the band (i.e., the total amount of hydrogen) being unchanged. Moreover, after growth of the crystal or annealing at about 1,000°C, the OH-vibrational spectrum reaches an equilibrium state during an extremely long time of the order of years [110]. The intensity ratio of two bands $R = I_{3,480}/I_{3,465}$ (where the subscripts denote the wavenumbers) slowly grows after annealing tending to a saturation during 10–15 months.

Because of an easy observation of the OH stretch mode by absorption spectroscopy, it serves as a tool for a quantitative determination of the hydrogen content required particularly for discussing the transport process. For today, in congruent undoped LiNbO₃ the most reliable averaged value of the cross-section is $\sigma_{\text{OH}} \approx 4 \times 10^{-19} \text{ cm}^{-2}$ obtained by different methods in [109, 111, 112]. Therefore, the concentration range of hydroxyl ions may be estimated approximately as $c_{\text{OH}} = c_{\text{H}} \approx 2 \times 10^{18} \text{ cm}^{-2} \alpha_{2.87 \mu\text{m}}$, where $\alpha_{2.87 \mu\text{m}}$ is the peak absorption value in cm^{-1} [100].

In as-grown congruent LiNbO₃ usually $\alpha_{2.87 \mu\text{m}} \approx (1-2) \text{ cm}^{-1}$, which corresponds to a hydrogen concentration in the range of 10^{18} cm^{-3} . Other estimates give a value $(3-6) \times 10^{19} \text{ cm}^{-3}$ [113, 114]. A change of the hydrogen content in the crystal is performed by different methods. The most commonly used method to enrich the hydrogen content is the annealing of a crystal in a water-vapour-rich atmosphere at temperatures between 400–700°C, sometimes at enhanced pressures. After a few hours of annealing, OH is distributed rather uniformly over the crystal bulk ([100] and references therein). A dehydration is achieved by vacuum annealing the crystal at temperatures of about 400°C. As this reduction procedure is accompanied by the formation of

bipolarons, as explained earlier, a subsequent annealing of the crystal in dry oxidizing atmosphere is required, to restore the initial optical transparency. Hydrogen (or hydroxyl) ions play a significant role in all processes related to the charge transport (photorefraction, thermal fixation of holograms, etc.), because, as shown in Sect. 3.2.1, the dark conductivity in undoped and low-doped LiNbO₃ crystals is controlled by the protonic conductivity in the range from room temperature to 1,000°C

2.4 Photorefractive and Relative Impurity Ions in the LiNbO₃ Lattice

As known, the dominant mechanism of the photorefraction in LiNbO₃ is the bulk photovoltaic effect. Therefore, the photorefractive properties of LiNbO₃ in the first instance are defined by the presence of the photovoltaic-active ions, belonging to multi-charge transition metal (TM) impurities, mainly Fe, and as well Cu, Mn, Ni, etc., [115]. In contrast, the TM impurity Cr is evidently not photovoltaic-active. Doping with any photorefractive ion provides in the visible range of the absorption spectrum a strong broad band responsible for the photoexcitation of the free electrons, which is a necessary condition for the realization of the photorefraction. Recently when developing the two-color holographic recording (so-called gating regime, see below) a definite, although an obscure role of some lanthanide ions ($\text{Ln}^{3+} = \text{Pr}, \text{Tb}$) in the photorefractive process was established, too. Of course, the main interest in LiNbO₃: Ln^{3+} is due to the possible laser action of Ln^{3+} ions and self-doubling of the generated frequency provided by the nonlinear optical properties of the LiNbO₃ host. In this section, we discuss the incorporation of the photorefractive impurities, mainly of Fe ions in the LiNbO₃ lattice. At the end the present state of studies of Ln^{3+} in LiNbO₃ is mentioned briefly. Particular attention is given to the influence of the crystal composition, i.e., the concentration ratio $[\text{Li}]/[\text{Nb}]$, on this ion incorporation, because, as shown later, this factor is crucial for the charge-transport scheme controlling the photorefractive process.

An incorporation of TM and Ln^{3+} ions into the LiNbO₃ lattice was a subject of long debates. As their concentration in the crystals is relatively low, X-ray diffraction methods cannot be applied for analyzing their lattice sites. The problem was solved using a combination of resonance and spectroscopic techniques, such as EPR, ENDOR (electron–nuclear double resonance), EXAFS (extended X-ray absorption fine structure), PIXE (particle induced X-ray emission), RBS (Rutherford backscattering spectroscopy), SSS (site-selective-spectroscopy), etc. (for references see the bibliographies in [115–123]). In principle, these ions might occupy either of three available octahedra sites (Li, Nb, and empty octahedron) or even interstitial sites. As the ionic radii of Nb^{5+} and Li^{+} are close, so from a qualitative reasoning of the charge compensation conditions, one could expect the incorporation of divalent impurity ions ($\text{Me}^{2+} = \text{Fe}^{2+}, \text{Cu}^{2+}$) onto the Li sites, of trivalent ones ($\text{Me}^{3+} = \text{Fe}^{3+}$,

Cr³⁺, Ln³⁺, etc.) equiprobably onto the Li and Nb sites (with a possible self-charge compensation of [Me_{Li}³⁺]^{••} by [Me_{Nb}³⁺]^{''}), and of Me⁴⁺ ions (e.g., Ti⁴⁺) dominantly onto the Nb sites. However, according to the data obtained with methods listed above, the impurity ions independently of their charge state are localized dominantly on the Li sites. Some authors [117] and [119] qualitatively explain it by a larger dimension of the Li octahedron discussed earlier. In [117], a qualitative correlation was found between the localization of an impurity ion Me in the LiNbO₃ lattice and the bondlength Me–O in the oxide of the given element. If this bondlength exceeds an average distance Nb–O in LiNbO₃ (of about 200 pm), then the Me ion incorporates onto the Li site. According to this qualitative criterion, there are only a few impurity ions (for example, Ta⁵⁺) substituting for Nb. Strictly speaking, this consideration is valid for the congruent, relatively low-doped LiNbO₃, because in what follows, other important factors governing the localization of impurity ions are the concentration ratio [Li]/[Nb] and the impurity concentration itself.

Among the TM photorefractive impurities the most strongest photovoltaic-active impurity Fe has been intensively studied in detail. The localization of Fe in LiNbO₃ was investigated by multiple methods; for the bibliography on spectral and resonance methods one may address the reviews [7, 55, 119, 122]. The impurity Fe exists in LiNbO₃ and LiTaO₃ in two charge states Fe²⁺ and Fe³⁺ and forms localized states in the gap, leading to a dichroic optical absorption spectrum (Fig. 2.11). The concentration ratio [Fe²⁺]/[Fe³⁺] in the congruent as-grown LiNbO₃ crystals is usually in the range of 0.1–0.2 and may be easily varied by an oxidation–reduction annealing [55, 115, 125].

The following absorption bands may be distinguished in the spectrum of LiNbO₃:Fe [124]. The high energy one at 3.1 eV overlapping the fundamental bandedge at 3.8 eV is assigned to the charge transfer from the π -oxygen orbitals (forming the valence band) to Fe³⁺ ions. A broad band with a maximum at about 2.6 eV corresponds to the intervalence transition Fe²⁺ – Nb⁵⁺ and is responsible for the photoexcitation of electrons to the conduction band formed by Nb⁵⁺ ions. The third pronounced band at 1.1 eV is attributed to an

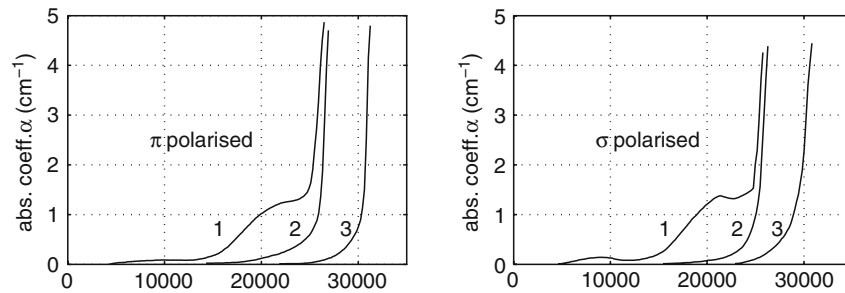


Fig. 2.11. Polarized absorption spectra of LiNbO₃ + 0.045 wt.% Fe₂O₃. (1) Crystal quenched from 1,100°C; (2) slow cooled and annealed at 600°C. (3) undoped LiNbO₃, data are taken from [124]

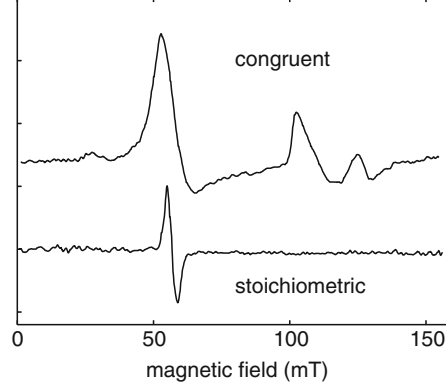


Fig. 2.12. Room temperature low field EPR spectra of Fe³⁺ in congruent and stoichiometric LiNbO₃, redrawn from [35]

internal d-d (⁵A → ⁵E) transition in Fe²⁺ ions. Additionally, one may detect two small lines at 2.55 and 2.95 eV owing to a spin-forbidden d-d transition of Fe³⁺ ions. The oscillator strengths of the bands 2.6 and 1.1 eV are 10⁻² and 4 × 10⁻⁴, respectively [115]. Therefore, the absorption bands 2.6 and 1.1 eV in LiNbO₃:Fe with intensities linearly scaling with the Fe²⁺ concentration, are tests for the presence of Fe²⁺. The spectrum of LiTaO₃:Fe is very similar to that of LiNbO₃:Fe except for slightly different spectral positions of the band peaks. Particularly, the peak of the band related to the intervalence transition Fe²⁺-Ta⁵⁺ is located at about 3 eV.

Fe³⁺ centers in LiNbO₃ and LiTaO₃ have axial symmetry, a characteristic EPR spectrum of Fe³⁺ in LiNbO₃ is shown in Fig. 2.12. As was unambiguously concluded, Fe²⁺ ions incorporate on Li sites [124, 126]. However, the incorporation of Fe³⁺ was a subject of a dispute. For example, some authors interpreted the EPR spectra of Fe³⁺ as evidences of its incorporation on the Nb sites [127–129]. Difficulties in the identification of EPR spectra of TM³⁺ (and Ln³⁺) ions in LiNbO₃ are due to the fact that the local environment at the Li and Nb sites is very similar. Only a combination of the EPR data with the EXAFS and ENDOR measurements [130–132], permitted to conclude that Fe³⁺ incorporate onto the Li sites in the congruent LiNbO₃.

As seen from Fig. 2.12, the EPR spectrum of Fe³⁺ in congruent LiNbO₃ is strongly asymmetric. LiNbO₃ crystals have the point symmetry *C*_{3v}, thus an axial Fe³⁺ center should exhibit *C*₃ symmetry. So, an asymmetrical shape of EPR spectra of Fe³⁺ in congruent LiNbO₃ (Fig. 2.12) was attributed to the existence of a large concentration of intrinsic defects (Nb_{Li}, V_{Li}, V_{Nb}) perturbing the crystal field and reducing its symmetry to *C*₁ [35]. In agreement with this conclusion it was found [35], that in near-stoichiometric LiNbO₃ crystals (grown by means of adding 6 wt.% K₂O into the melt [34]) the Fe³⁺ EPR spectrum becomes more symmetrical (Fig. 2.12). Therefore in a stoichiometric LiNbO₃ crystal, free of defects, a more symmetrical shape of the Fe³⁺-EPR

spectrum fits the required C_3 symmetry of a nonperturbed crystal field. It should be emphasized that in the stoichiometric crystals Fe impurity keeps its traditional state Fe^{2+} and Fe^{3+} , the Fe^{2+} ion occupying the Li site again. However the concentration ratio $[\text{Fe}^{2+}]/[\text{Fe}^{3+}]$ in as-grown SLN:Fe crystals is lesser than in CLN:Fe, so the former crystals are weakly colored. For a detailed bibliography on the fundamental resonance studies in SLN doped with TM^{3+} , see for example [121, 123].

Analyzing the Fe^{3+} EPR spectrum in near-stoichiometric $\text{LiNbO}_3\text{:Fe}$ crystals grown with K_2O in the melt, Malovichko et al. [133] found that additional to the traditional $\text{Fe}_{\text{Li}}^{3+}$ centers, one may identify two new axial centers related to Fe^{3+} with the Spin-Hamiltonian parameters strongly differing from those in congruent crystals (e.g., $b_2^0 = 0.1768 \text{ cm}^{-1}$ for $\text{Fe}_{\text{Li}}^{3+}$, whereas for the two new centers $b_2^0 = 0.0495$ and 0.0688 cm^{-1} [133]). They suggested that these new lines could be assigned to $\text{Fe}_{\text{Nb}}^{3+}$ and $\text{Fe}_{\text{Nb}}^{3+}\text{-K}^+$ centers (where K ions, whose concentration in these crystals is in the range of 10^{-2} , are located either on the Li sites or within the empty O octahedra). Therefore, in the stoichiometric LiNbO_3 a partial incorporation of Fe^{3+} on the Nb sites was assumed. Following Donnerberg et al. [134] the self-charge compensation $[\text{Fe}_{\text{Li}}^{3+}]^{\bullet\bullet} - [\text{Fe}_{\text{Nb}}^{3+}]''$ may occur. Similarly, in the stoichiometric $\text{LiTaO}_3\text{:Fe}$ the existence of Fe^{3+} centers on Ta sites was recently deduced from EPR/ENDOR studies [135].

Keeble et al. [136] investigated the EPR spectra of Fe^{3+} in the nearly stoichiometric $\text{LiNbO}_3\text{:Fe}$ grown by the double-crucible method. A narrowing of the linewidth, a more symmetrical shape of the spectrum as well as Spin-Hamiltonian parameters very close to those in SLN:Fe, containing K admixture, were found [34, 133]. However, Keeble et al. [136] contend that the information obtained from a modified Fe^{3+} EPR spectrum is inadequate to deduce the alteration of the Fe^{3+} lattice sites. Anyhow, a possibility of the formation of $\text{Fe}_{\text{Nb}}^{3+}$ in SLN crystals is of principal importance. As known, $\text{Fe}_{\text{Li}}^{3+}$ serves in the congruent LiNbO_3 as the dominant electron trap. Thus, an alteration of the Fe^{3+} lattice site could fundamentally affect the charge transport scheme and possibly account for specials of the photorefractive process in SLN. This problem will be discussed in the appropriate Sects. 4.1 and 4.2.2.

Another photorefractive impurity studied in more or less detail in LiNbO_3 is Cu [115, 137]. Copper exists in LiNbO_3 in the charge states Cu^{2+} and Cu^+ . The absorption spectrum of $\text{LiNbO}_3\text{:Cu}$ (Fig. 2.13) reveals two bands. One of them overlapping the bandedge and stretching far into the visible is attributed to the intervalence transition $\text{Cu}^+ - \text{Nb}^{5+}$. By means of an oxidation-reduction treatment its peak position was established to be at 3.3 eV [115]. Another band at about 1.2 eV is assigned to the transition ${}^2\text{E} \rightarrow {}^2\text{T}_2$ of Cu^{2+} ions. In photorefractive $\text{LiNbO}_3\text{:Mn}$ crystals the absorption spectrum exhibits two broad bands at about 2.2 and 1 eV [138, 139]. According to ENDOR studies [140] Mn^{2+} ions occupy Li sites. The appropriate bibliography on other photorefractive impurities in LiNbO_3 is few in number [55].

Although Cr^{3+} is not a photovoltaic center, its spectral characteristics in LiNbO_3 are worthy of a short discussion, because they are strongly affected

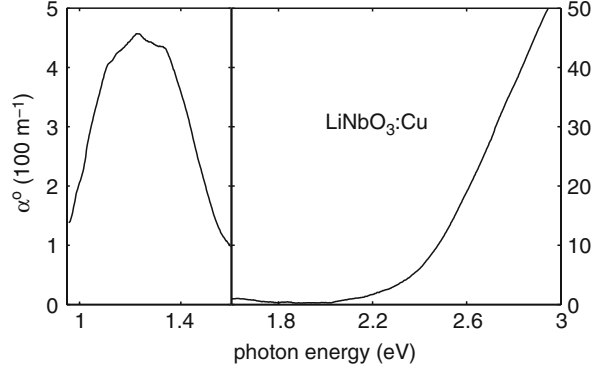


Fig. 2.13. Absorption coefficient α vs. photon energy for ordinarily polarized light in Copper-doped LiNbO₃, data taken from [137]

by the stoichiometry. A specific of the incorporation of Cr³⁺ ions into LiNbO₃ is the formation of several axial nonequivalent centers at the same lattice site, caused by a nonequivalent local environment. Difficulties in the interpretation of the EPR- and emission/absorption spectra are the cause of an extremely long discussion on the Cr³⁺ ion localization in LiNbO₃ [121,141–143]. According to combination of EPR, ENDOR, EXAFS and other data, in congruent crystals Cr³⁺ ions incorporate onto the Li site, at least in low-doped crystals. EPR studies in congruent LiNbO₃:Cr additional to the main axial Cr_{Li}³⁺ center detected several nonequivalent Cr³⁺ centers – dimer or even trimer complexes, satellite Cr centers and even nonaxial centers, which were accounted for by an interaction of Cr_{Li}³⁺ with the compensating intrinsic defects [121,144]. In near-stoichiometric crystals the linewidths of the Cr³⁺ EPR spectra are narrowed, the satellites disappeared and the spectrum is more symmetric [121,142]. The EPR and ENDOR studies in these crystals [142] revealed a family of new centers attributed to Cr³⁺ incorporation onto an Nb site. Regarding the compensation mechanism of the [Cr_{Nb}]^{''} center, a compensation by H⁺ ions was assumed, whereas the self-compensation [Cr_{Nb}]^{''} – [Cr_{Li}]^{••} was ruled out [142]. A similar conclusion was drawn from the spectroscopic measurements (absorption/emission spectra, site-selective-spectroscopy, etc.). As known, Cr doping in LiNbO₃ produces broad absorption bands related to vibronic transitions $^4A_2 \rightarrow ^4T_1$ and $^4A_2 \rightarrow ^4T_2$ with maxima at about 500 and 650 nm, respectively [145]. At the long wavelength shoulder of the latter band a group of weak lines exists in the range from 720 to 750 nm. They are related to $^4A_2 \rightarrow ^2E$ transitions. This excited final state is the origin of radiative transitions, the so-called R-lines. A great number of data was recently presented on the absorption/emission spectra, particularly in the R-line range in near-stoichiometric LiNbO₃:Cr crystals, [146–152]. At increased Li content, additionally to the initial strong emission bands two more at longer wavelengths appear, whose intensities increase with increasing Li content, whereas the intensities of the

initial bands decrease. A correlation to the EPR and ENDOR data led to the conclusion that these variations in emission spectra are associated with the appearance of $\text{Cr}_{\text{Nb}}^{3+}$ and their coupling to other nonequivalent Cr^{3+} centers, e.g., the formation of a dimer $\text{Cr}_{\text{Nb}}^{3+}\text{--Cr}_{\text{Li}}^{3+}$ [148].

Surprisingly in the isostructural LiTaO₃ crystal so far no evidences have been found of an impact of $[\text{Li}]/[\text{Ta}]$ on the incorporation of TM ions. Some researchers performed detailed EPR studies of Fe^{3+} and Cr^{3+} in nearly stoichiometric LiTaO₃ crystals grown by the double-crucible method [153, 154]. The Spin–Hamiltonian parameters calculated for both centers at 300 K are very close to those in congruent material. Hence, it was concluded that both in the stoichiometric and congruent LiTaO₃ crystals Fe^{3+} and Cr^{3+} ions incorporate on Li sites.

We now briefly dwell on the incorporation of the lanthanide ions (Ln^{3+}) into the LiNbO₃ lattice. As mentioned earlier, according to recent measurements with various methods, all Ln^{3+} ions occupy the Li sites (for references see, e.g., [120]). Unlike TM ions, Ln^{3+} ions in Li octahedra are off-centered with respect to the regular Li site by 30–50 pm, the shift being dependent on the Ln^{3+} ionic radii, see Fig. 2.14. A speciality of the axial Ln^{3+} centers in LiNbO₃, like Cr^{3+} ions is the coexistence of several nonequivalent centers at the same lattice site. Practically, the most interesting material is LiNbO₃:Nd³⁺ in which a laser excitation, even with the self-frequency doubling has been reported since long ago [155–158]). The emission spectrum in this crystal reveals a band corresponding to a radiative ${}^4\text{I}_{\frac{9}{2}} \rightarrow {}^4\text{F}_{\frac{3}{2}}$ transition (860–960 nm), whose fine structure was formerly assigned to the existence of three nonequivalent Nd³⁺ centers [159, 160] and then refined to six ones [161], for details see Fig. 2.15. At early stages, these nonequivalent Ln^{3+} centers were sometimes interpreted as Nd³⁺ both on the Li and Nb sites [159, 162]. After convincing arguments in favor of the Ln^{3+} localization on Li sites, all these six centers were related to Nd_{Li}. The fine structure of the excitation spectrum

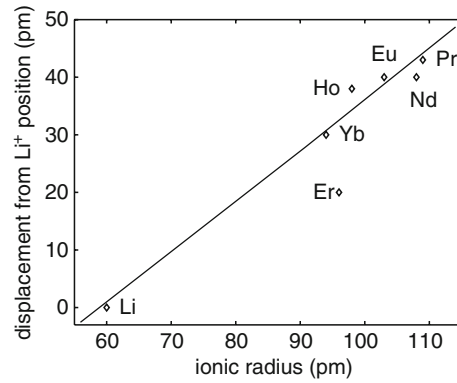


Fig. 2.14. Displacement from the Li^+ position in LiNbO₃ vs. the ionic radius of active RE^{3+} ions, data taken from [120]

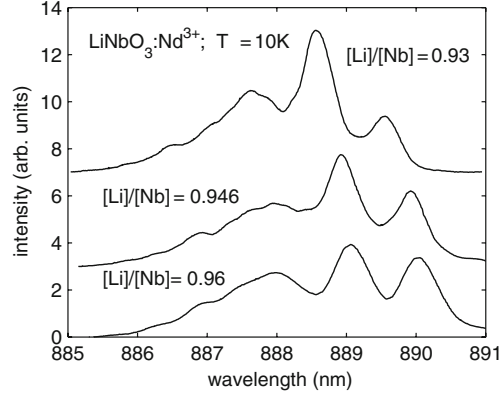


Fig. 2.15. Low temperature emission spectrum of the ${}^4F_{3/2} \rightarrow {}^4I_{9/2}$ transitions of Nd^{3+} ions in LiNbO_3 , data taken from [120]

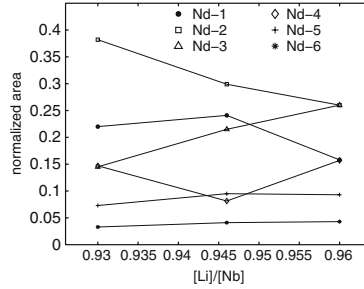


Fig. 2.16. Compositional dependence of the intensities of the six centers of the ${}^4F_{3/2} \rightarrow {}^4I_{9/2}$ transitions shown in Fig. 2.15, data taken from [120]

is sensitive to the crystal stoichiometry. As seen in Fig. 2.15 a slight variation in the $[\text{Li}]/[\text{Nb}]$ ratio, achieved in [161] by controlling the $[\text{Li}]/[\text{Nb}]$ ratio in the melt, affects the strengths of some lines, the spectral positions of the lines being almost unchanged. More quantitative information is given in Fig. 2.16, where the intensities in terms of the normalized area for each center as a function of the $[\text{Li}]/[\text{Nb}]$ ratio is presented. The results of the spectroscopic studies in accordance with the EXAFS data [163, 164] indicate that Nd^{3+} ions keep the Li sites independently of the crystal stoichiometry. Comparative studies of Nd^{3+} in near-stoichiometric and congruent LiNbO_3 crystals were performed by the EPR method [165]. The Nd^{3+} -EPR band in congruent crystals is too broad to analyze its fine structure. An enormous narrowing of the EPR lines in stoichiometric $\text{LiNbO}_3:\text{Nd}$ permitted to distinguish four nonequivalent centers, one of them being axial with a C_3 symmetry and others with the lower symmetry C_1 .

An impact of the crystal stoichiometry on the excitation spectra was found also for Er^{3+} ions. As known, Er doping is of practical interest due to possible

laser action at technically important wavelengths of about 1,500 nm (0.83 eV). Additionally, the Er³⁺ ion offers a variety of other transitions and excitation possibilities in the spectral ranges 2.26, 2.55, and 2.75 eV. According to detailed studies by EXAFS, RBS, ion-beam channeling methods, and others (for references see, e.g., [166]) the Er³⁺ ion occupies the Li site forming several non-equivalent centers. For example, several groups [167–169] when investigating the emission range at 2.26 eV, i.e., the transition $^4S_{3/2} \rightarrow ^4I_{15/2}$, with the use of site-selective-spectroscopy found in SLN:Er³⁺ not less than 11 resolved peaks belonging to optically different Er³⁺ centers and in CLN:Er³⁺ even more (13 ones). The widths of all lines in SLN:Er³⁺ are strongly narrowed as compared to CLN:Er³⁺ and the line intensities are noticeably redistributed [166, 168], like in LiNbO₃:Nd³⁺. Similar results were obtained for Eu³⁺ [170].

In summary, at present there are convincing data indicative of an alteration of TM (TM³⁺ = Fe³⁺, Cr³⁺) lattice site in the stoichiometric LiNbO₃, whereas Ln³⁺ ions seem to keep the Li sites independently of the crystal stoichiometry.

2.5 Optical-Damage-Resistant (Non-Photorefractive) Impurity Ions in the LiNbO₃ Lattice and Their Impact on the Incorporation of Other Impurity Ions

The effect of optical-damage-resistant impurities on the optical properties of LiNbO₃ is rather specific. The main role of these ions seems to vary the amount of the Nb antisites in the crystal. It is a reason of a pronounced dependence of many optical properties controlled by the intrinsic defects, on the doping with the optical-damage-resistant ions.

2.5.1 Incorporation of the Optical-Damage-Resistant Ions into the Lattice

As mentioned in Chap. 1, the most important practical task with respect to optical applications of LiNbO₃ is an improvement of its optical stability under intensive light, in particular a protection against the optical damage. The most efficient and technologically easy method is doping LiNbO₃ with relatively high concentrations of optical-damage-resistant impurities. The first optical-damage-resistant composition found was LiNbO₃:Mg, where a reduction of the optical damage was noticed when doping with 4.6% Mg [171]. In more details LiNbO₃:Mg was studied later [76, 172, 173]. These authors accounted for the optical damage resistance an increased photoconductivity and detected a critical concentration of about 5 mol.% MgO for the congruent melt, referred to as a *threshold*, above which the optical damage drastically falls off by more than two orders of magnitude. Several optical properties as well revealed anomalies at about this critical concentration. Additionally, it was found by

Sweeney et al. [76] and confirmed by Feng et al. [174] that this threshold is lowered to 3% in a crystal grown from a melt with a ratio of $[\text{Li}]/[\text{Nb}] = 1.2$. Just these results led to the assumption that Mg doping effects indirectly and is related to an action of Mg^{2+} ions on the intrinsic defect structure.

Starting from a chemical analogy of Zn^{2+} ions to Mg^{2+} ions a significant reduction of the optical damage was found in $\text{LiNbO}_3\text{:Zn}$ [175, 176], with a particularly strong effect for ZnO concentrations exceeding 7 mol.% for the congruent melt. Zhang et al. [177] observed in congruent $\text{LiNbO}_3\text{:Zn}$ a lower threshold of about 6 mol.% ZnO. The dependencies of many optical properties of $\text{LiNbO}_3\text{:Zn}$ were very similar to those of $\text{LiNbO}_3\text{:Mg}$, as they revealed anomalies in the concentration range at about 7 mol.% ZnO. This similarity of properties of both $\text{LiNbO}_3\text{:Mg}$ and $\text{LiNbO}_3\text{:Zn}$ crystals permitted to conclude the existence of an optical-damage-resistant *family* of ions and to predict other members of this family on the base of the qualitative crystal-chemistry *principle of the diagonal rows* within the periodic table of the elements. These are in the first instance the trivalent ions In^{3+} and Sc^{3+} . Optical damage resistance was actually proved in $\text{LiNbO}_3\text{:In}$ [178–180] and $\text{LiNbO}_3\text{:Sc}$ [181, 182]. In these cases, a drastic decrease of the photorefraction and anomalies of optical properties are observed at concentration below 2 mol.% oxides (i.e., 4 at.%) in the melt for congruent crystals. Recently, two new optical-damage-resistant impurities, Hafnium (Hf) and Zirconium (Zr), were found [183–186], whose influence on the photorefraction and optical properties qualitatively reminds of that of the former optical-damage-resistant ions. After subsequent refinement, the threshold concentration of Hf was established below 2% [187]. The most recently studied optical-damage-resistant impurity ion is Zr^{4+} [188], although discovered already 3 years earlier [183]. In $\text{LiNbO}_3\text{:Zr}$, the photorefraction drastically drops at a ZrO_2 concentration less than 2 mol.%. So, at present the family of the optical-damage-resistant impurities includes divalent (Mg, Zn), trivalent (In, Sc) and tetravalent (Hf, Zr) ions. Note that Hf is a full analog of Zr; it belongs to the group of scattered elements (Rb, Ga, Ge, etc.), forms no natural minerals and persists always as an admixture in zirconium-based natural minerals. The term family is appropriate, because an impact of these impurities on various properties of LiNbO_3 is qualitatively very similar in spite of different valency.

In LiTaO_3 doping with Mg lowers the photorefraction as well [189]. One more impurity suppressing the optical damage in LiNbO_3 is Na [190], but the results are still ambiguous. There are indirect indications on a similar role of Ga doping in waveguiding structures in $\text{LiNbO}_3\text{:Mg}$ [191]. Other impurity ions lowering the optical damage in the LiNbO_3 waveguides are indiffused monovalent Ag [192] and protons [193].

In contrast to LiNbO_3 doped with the photorefractive impurities described and discussed in many monographs and reviews, material on optical damage resistance in LiNbO_3 has been summarized so far only in two reviews [194, 195]. So, we discuss the optical-damage-resistant impurities in LiNbO_3 in more detail than the well-known photorefractive ones.

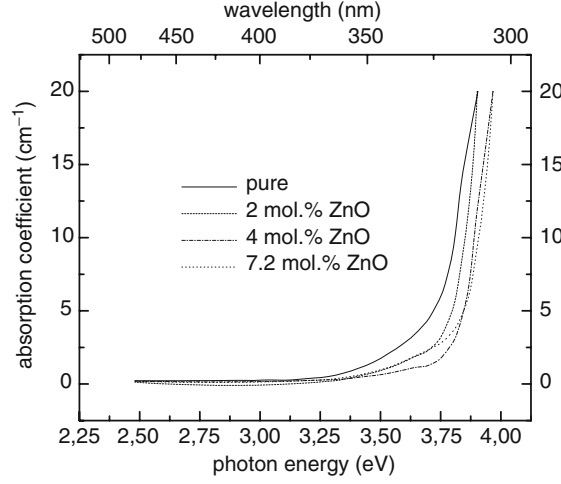


Fig. 2.17. Shift of the absorption edge of Zn-doped LiNbO₃, redrawn from [196]

At first a great similarity of the properties of optical-damage-resistant LiNbO₃ crystals manifests in their optical absorption spectra exemplified by LiNbO₃:Zn (Fig. 2.17). Doping with any member of this family (Mg [197,198], Zn [196], In [199], Sc [181], Hf [183], and Zr [183,188]) induces no changes within the whole transparency range 0.35–4 μm except for a slight shift of the UV bandedge towards shorter wavelengths. The optical inactivity of these impurities is the basis for the great interest on them from the point of view of optical applications.

As mentioned earlier, a drastic decrease of photorefraction at impurity concentrations exceeding certain thresholds, constant for a given impurity, is accompanied by anomalies (extremes, kinks, steplike changes, etc.) of optical properties. Non-monotonic dependencies of the refractive indices and phase-matching temperatures on the concentrations of the optical-damage-resistant impurities will be described in Chap. 6 devoted to the characterization of the optical-damage-resistant LiNbO₃ compositions. Now we exemplify the threshold behavior of optical parameters by the steplike shift of the OH absorption band in LiNbO₃:Zr, see Fig. 2.18. Such a steplike shift of the IR band is observed in all optical-damage-resistant crystals, the value of the shift decreasing from di- to tetravalent ions, see Table 2.4.

Before discussing the threshold concentrations of optical-damage-resistant impurities and the concentration dependencies of the parameters, the following remark is worthy of noting. There are two ways to specify the impurity content, which with LiNbO₃:Mg as an example looks as follows:

$$c_{\text{Mg}}^{(1)} = [\text{MgO}] / ([\text{Li}_2\text{O}] + [\text{MgO}] + [\text{Nb}_2\text{O}_5]),$$

$$c_{\text{Mg}}^{(2)} = [\text{MgO}] / ([\text{LiNbO}_3] + [\text{MgO}]).$$

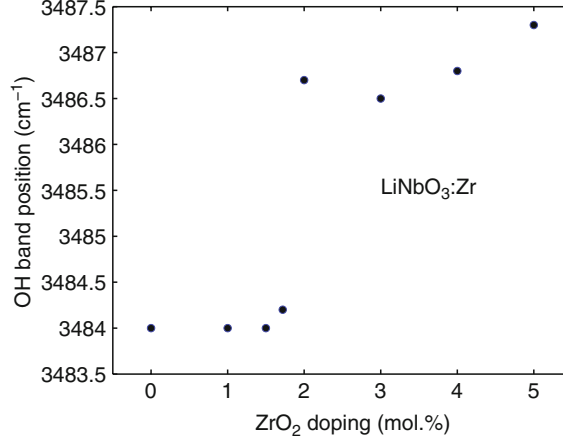


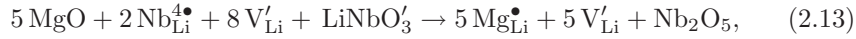
Fig. 2.18. Position of the OH stretch mode band as a function of the ZrO₂ doping in LiNbO₃, data taken from [188]

The first definition is adapted to the phase diagram Li₂O–MgO–Nb₂O₅ [200, 201]. These values are different, for example for usual MgO concentration $c_{\text{Mg}}^{(2)} \approx 2 c_{\text{Mg}}^{(1)}$ [202]. Sometimes a scatter in the threshold concentration values and in concentration dependencies of various parameters is due to an ambiguity in the definition of the concentrations.

The effects of optical-damage-resistant impurities on numerous properties of LiNbO₃ are an increase of T_c (Fig. 6.3) and of the crystal density in LiNbO₃:Mg [200] and LiNbO₃:Zn [203], an increase of the temperature of the noncritical phase synchronism [173, 175, 176, 182], a UV shift of the optical absorption band (Fig. 2.17), qualitatively reminds us the results of increasing Li content, i.e., of an ordering of the structure. Particularly, it concerns the blueshift of the absorption edge (Fig. 2.17), because this shift in Li-enriched LiNbO₃ was attributed to the disappearance of intrinsic defects and subsequent hardening of the structure [204]. In the framework of the current model of the defect structure, an impact of the optical-damage-resistant ions resembles a decreasing Nb_{Li} content. Thus, it was a priori explained by a removal of Nb_{Li} from the lattice due to the entering the impurity ions onto Li sites.

We now trace the development of the proposed scenario of entering the optical-damage-resistant dopants into the LiNbO₃ lattice and their action on the intrinsic defect structure. As mentioned above, according to the current conclusion, the preferable sites of almost all impurity ions are the Li octahedra. In the case of LiNbO₃:Mg [201, 205, 206] the a priori expected incorporation of these ions onto Li sites was convincingly proved by different methods. A precise chemical analysis in LiNbO₃:Sc [207] and EXAFS, ion beam and hyperfine interaction methods in LiNbO₃:Hf [208, 209] led to the same conclusion for low Sc and Hf concentrations.

However, the incorporation mechanism and in particular its influence on the threshold concentrations was and still remains debatable. Because the threshold concentration of Mg (5.5%) in congruent crystals is close to the Nb_{Li} content [41], it was reasonable to relate it to a complete removal of Nb_{Li} from the lattice [134,205,210,211]. This assumption was supported by the fact that the threshold Mg concentration was lowered with increasing Li content in crystals [76,174,212]. From the same viewpoint, the most energetically favorable solution reactions underlying the different threshold concentrations for di- and trivalent impurities are according to [202]



As seen from this simplified presentation, the number of trivalent cations required for a removal of Nb_{Li} is less than that of divalent ones, that means the threshold for the former is lower, because the ratio of the replacement is decreased from 5/2 to 5/3.

The relation of the threshold concentrations to the disappearance of Nb_{Li} seemed to be supported by spectroscopic tests described in Sect. 2.2. Recall that a reduction of Li-deficient (congruent) LiNbO₃ is accompanied by the appearance of a broad absorption band in the visible (Fig. 2.6) attributed to the formation of a bipolaron (Nb_{Nb}-Nb_{Li})²⁻ [55]. The low temperature illumination of reduced crystals, leading to a dissociation the bipolaron by (2.10) and giving a characteristic 10-line EPR spectrum (Fig. 2.4) serves as a test for the presence of Nb_{Li}. Such experiments were performed in LiNbO₃:Mg [76], LiNbO₃:Zn [56,78] and LiNbO₃:In [179] crystals with impurity concentrations below and above the thresholds. The results are exemplified by LiNbO₃:In. For impurity concentrations below the thresholds in all these crystals the optical absorption spectra (Fig. 2.19, left) were qualitatively similar to those in congruent crystals (Figs. 2.4 and 2.6), thus evidencing the existence of Nb_{Li}. On the other hand, at impurity concentrations exceeding the thresholds, the

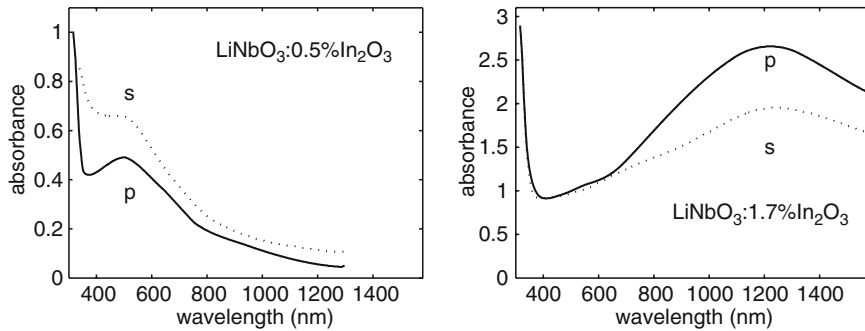


Fig. 2.19. Polarized absorbance (s, p) of reduced LiNbO₃ doped with indium below the threshold (*left*) and above (*right*)

spectrum of reduced material looks quite different (Fig. 2.19, right) and does not respond to illumination. The broad band at about 0.95 eV (1,200 nm) was assigned to a free small polaron $\text{Nb}_{\text{Nb}}^{+4}$ [77,78]. So, these results were indicative of missing Nb_{Li} for optical-damage-resistant impurity concentrations above the thresholds.

However, further studies in $\text{LiNbO}_3\text{:Mg}$ [201,206] revealed that the origin of the threshold required a refinement. A precise chemical analysis have shown that the ratio $[\text{Li}]/[\text{Nb}] = 0.94$ in $\text{LiNbO}_3\text{:Mg}$ remains constant up to 2–3% MgO, whereas a further increase of the impurity concentration diminishes it [201,206]. Both research groups started from the assumption of an occupation of 100% of oxygen sites, they accounted for a decrease of $[\text{Li}]/[\text{Nb}]$ by an increase of the Li vacancy concentration. In the framework of the Li site vacancy model, the authors of [206] proposed a two-step scheme of the Mg incorporation, accordingly to which Nb antisites are completely substituted by Mg ions at $[\text{Mg}] \sim 2\%$, whereupon Mg ions substitute for the regular Li ions [206]. The authors assumed that the appearing surplus of Mg_{Li} is compensated by V_{Li} , so at this stage their concentration increases again. Grabmaier et al. [201] discussed their data in terms of the Nb site vacancy model, so their interpretation was qualitatively different. Similar precise chemical analysis in $\text{LiNbO}_3\text{:Sc}$ [207] discussed in the same way evidenced that Nb antisites are removed at 2% Sc, afterwards Sc substitutes for the regular Li ions. Table 2.2 presents a variation scheme of the defect structure of $\text{LiNbO}_3\text{:Mg}$ following the two-step scheme proposed by Iyi et al. [206].

However, the calculations of [202] show that such a two-step Mg incorporation is energetically unfavored, therefore a more probable process seems to be a simultaneous substitution of Nb antisites and regular Li_{Li} ions by Mg. The same conclusion was drawn in [211]. So, up to now it is unclear whether Nb antisites disappear from the lattice at the threshold concentration in its traditional meaning, or at a lower concentration referred sometimes to as *the first threshold* [213]. According to the conclusions of [202] and [211] Nb antisites do exist in the crystal up to the usual thresholds of the optical-damage-resistant ions, although the process of substitution and the compensation mechanism vary in different concentration ranges. As described above, the existence of Nb antisites up to the threshold is supported by spectroscopic tests.

In addition to a removal of Nb antisites at threshold concentrations, the model calculations [55,134] and indirect indications from NMR-spectra of the

Table 2.2. Incorporation of Mg ions into congruent LiNbO_3 (deduced from [206]). The symbol \square denotes the Li vacancy

% MgO	Formula (Li site vacancy compensation)
0.0	$[\text{Li}_{0.95}\text{Nb}_{0.01}\square_{0.04}][\text{Nb}]\text{O}_3$
3.0	$[\text{Li}_{0.94}\text{Mg}_{0.03}\square_{0.03}][\text{Nb}]\text{O}_3$
8.0	$[\text{Li}_{0.84}\text{Mg}_{0.08}\square_{0.08}][\text{Nb}]\text{O}_3$
28.0	$[\text{Li}_{0.79}\text{Mg}_{0.21}][\text{Nb}_{0.931}\text{Mg}_{0.069}]\text{O}_3$

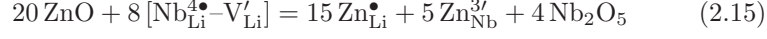
Table 2.3. Incorporation of Zn ions into congruent LiNbO₃ [215–217]. The symbol \square denotes the Li vacancy

Zn (at.%)	Formula
0.0	[Li _{0.940} Nb _{0.012} \square _{0.048}][Nb]O ₃
2.87	[Li _{0.908} Nb _{0.007} Zn _{0.029} \square _{0.056}][Nb]O ₃
5.2	[Li _{0.898} Zn _{0.052} \square _{0.05}][Nb]O ₃
7.6	[Li _{0.939} Zn _{0.06}] \square _{0.001}][Nb _{0.98} Zn _{0.015} \square _{0.005}]O ₃
8.2	[Li _{0.95} Zn _{0.06}][Nb _{0.98} Zn _{0.022}]O ₃

Mg nuclei [214] suggested a possibility of a partial incorporation of optical-damage-resistant ions onto the Nb sites after a complete removal of Nb_{Li} defects. From this viewpoint, the microscopic origin of the threshold concentration was investigated by structure studies in LiNbO₃:Zn and LiNbO₃:In [215–218]. The Zn impurity is the most convenient one for such studies, because it has the largest threshold (7.5%) among all damage-resistant impurities, thus providing the highest faithfulness of the estimates. The precise X-ray diffraction measurements were performed in single crystals and powders [215, 216]. Data on the occupancy coefficients of atoms in LiNbO₃:Zn obtained from the refinement of the structures, led to the chemical formulas of LiNbO₃:Zn shown in Table 2.3; Zn_{Li} was assumed to be compensated by Li vacancies. The main conclusion drawn from Table 2.3 is that at Zn concentrations close to the thresholds and above them, Zn ions incorporate partially onto the Nb sites. This conclusion was supported for LiNbO₃:8%Zn single crystals by neutron diffraction studies [217]. Similar results were obtained in LiNbO₃:In [218]. At a concentration of about 2.7 at.% (above the threshold) In ions were found on both the Li and Nb sites.

Therefore, these structure measurements established unambiguously the microscopic origin of the threshold concentrations, namely, the association of the threshold to a partial incorporation of the optical-damage-resistant ions onto the Nb sites. This fundamental unambiguous conclusion is obviously valid for all optical-damage-resistant dopants. Additionally to direct structure investigations in LiNbO₃:Zn and LiNbO₃:In [215–218], in Hf-doped LiNbO₃ the indirect data on the ion-beam and hyperfine interaction methods are evidences of the incorporation of Hf ions onto both Li and Nb sites in highly-doped crystals [209, 219]. The incorporation mechanism for the Hf impurity depends on the crystal stoichiometry: in congruent Hf_{Nb} were found at [HfO₂] = 6 mol.% (in the melt) and in near-stoichiometric LiNbO₃ at [HfO₂] as low as 1%. This is in accordance with the well-known result on decreasing Mg threshold concentration in Li-enriched crystals [76, 174].

An incorporation of impurity ions simultaneously onto both cation sites requires a modification of the charge compensation conditions (2.13), (2.14). The model calculations [134] showed that for this case a self-charge compensation mechanism may occur. For a two-valence ion it looks as follows:



and requires a concentration ratio of the self-compensating ions $[\text{Zn}_{\text{Nb}}^{3'}/[\text{Zn}_{\text{Li}}^{\bullet}] = 1 : 3$. As seen from Table 2.3, this ratio is fulfilled in a rough approximation for LiNbO₃:Zn with the above-threshold concentrations 7.6% and 8.2% Zn, hence the mechanism (2.15) may be assumed. As it does not require more Li vacancies for the charge compensation, the threshold impurity concentration is followed by the disappearance of V_{Li} from the lattice. Chemical microanalysis measurements in LiNbO₃:Mg [201,206] also indirectly indicate an anomaly in the Li vacancy content at the threshold Mg concentration. Figure 2.20 presents a scheme of the defect structure variation produced by Zn doping based on the data of Table 2.3 [215–217]. Additionally, within certain assumptions for LiNbO₃:Zn and following the two-step mechanism of Mg incorporation [206] it was concluded that Nb antisites disappear from the lattice in the concentration range $3\% < \text{Zn} < 5\%$ (Table 2.3).

As seen from Tables 2.1 and 2.2 optical-damage-resistant ions Mg and Zn at relatively low concentrations may be regarded as controllers of the Nb_{Li} content, so their effect is qualitatively analogous to a Li enrichment. This is in a qualitative consistence, with a similarity between the blueshift of the band-edge in LiNbO₃:Zn (Fig. 2.17) [220] or LiNbO₃:Mg [197,198] and in Li-enriched crystals [204]. This shift saturates at $[\text{Zn}] \sim 4\%$, which according to (Fig. 2.20) corresponds to a disappearance of $[\text{Nb}_{\text{Li}}]$. These qualitative considerations and the results in Fig. 2.20 are consistent with the data on the lattice parameters in LiNbO₃:Zn vs. the Zn concentration Fig. 2.21 [221]. This dependence deviates from Vegards rule, expecting a smooth variation of the lattice parameters when increasing the concentration of a substituting impurity. Plateaus of the lattice parameters a and c as well as the volume V vs. $[\text{Zn}]$ at low Zn concentrations transform to a steep slope at above-threshold Zn concentrations. Very similar plots were obtained for LiNbO₃:Zn [177,203], where these plateaus in the low concentration range (2–3% Zn) are more pronounced, so a and c even

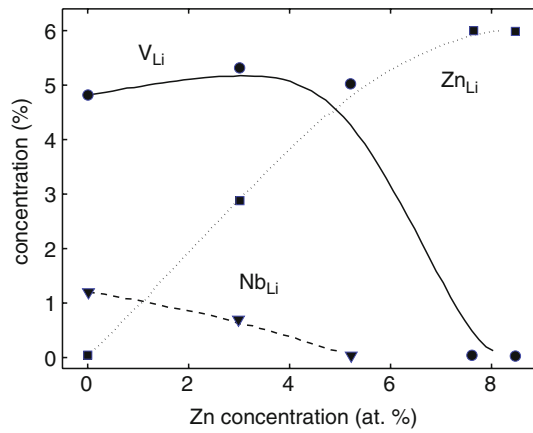


Fig. 2.20. Intrinsic defects in Zn-doped LiNbO₃ vs. Zn concentration

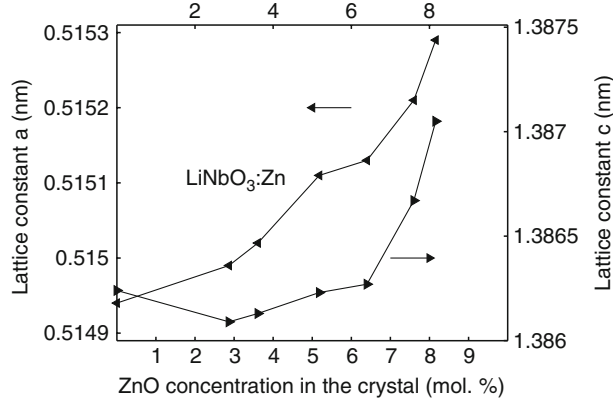


Fig. 2.21. Lattice constants of Zn-doped LiNbO_3 vs. ZnO concentration in the crystal. Data were taken from Abdi et al. [221]

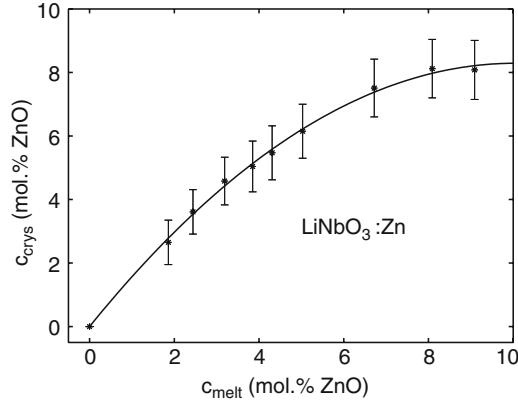


Fig. 2.22. Variation of the Zn concentration in the crystal as a function of the ZnO in the melt. The curve is a fit according to the equation in the text. Data were taken from Schlarb et al. [220]

tend to decrease. These plateaus argue of a hardening of the lattice due to a decreasing V_{Li} content and lowering Coulomb repulsion. Indeed, according to [203] the crystal density of $\text{LiNbO}_3\text{:}2\%\text{Zn}$ noticeably grows with respect to the undoped crystal ($4.72\text{--}4.62\text{ g cm}^{-3}$, respectively), whereas at further $[\text{Zn}]$ increasing it varies slightly.

As repeatedly mentioned earlier, the preferable site of all impurity ions in LiNbO_3 , is the Li octahedron. At low concentrations, the optical-damage-resistant ions incorporate in LiNbO_3 comparatively easy with distribution coefficients in the range $K_{\text{eff}} = 1.2\text{--}1.3$; at higher concentrations K_{eff} decreases to 1 for MgO [200] and ZnO [220] in the range 5–6 mol.% and to about 0.9 for In_2O_3 in the range 1.5–2 mol.% [222]. However, at above-threshold concentrations K_{eff} gradually saturates. This is illustrated in Fig. 2.22, which

presents the dependence of the Zn concentration in the crystal c_{crys} on the concentration in the melt c_{melt} . The dependence is described with good accuracy by $c_{\text{crys}} = 1.649 c_{\text{melt}} - 0.082 c_{\text{melt}}^2$ [220]. One may see, that above the threshold the Zn concentration is close to a tolerable limit, because increasing c_{melt} does not increase c_{crys} more, as if an impurity incorporation onto both cation sites brings a given crystal lattice to a critical state. In contrast to di- and trivalent ions, the distribution coefficient for Zr seems not to depend on the concentration being of about 1.0 for the doping range from 1 to 5 mol.% ZrO₂ [188].

He et al. [223] discussed the incorporation and the thresholds of the optical-damage-resistant ions in terms of the influence of these ions on the chemical bonds within LiO₆ and NbO₆ octahedra. The consideration is based on the semi-empirical bond-valence approach, for references see, e.g., [224], according to which the stability of a structure may be established from calculations of the bond-valence sum for a given cation in a given environment. Within this concept, the stability of the LiNbO₃ lattice decreases with increasing optical-damage-resistant ion concentrations, so the location of such an ion is changed from an Li to Nb site provided that certain threshold of a global lattice instability is exceeded. Based on the traditional Nb_{Li}-V_{rmLi} concept and some experimental data, He et al. [223] deduce reasonable values of thresholds for di-, tri-, and tetravalent optical-damage-resistant impurities. Summarizing the data on the threshold concentrations of optical-damage-resistant impurities in congruent LiNbO₃ crystals, one may conclude that a more or less substantial microscopic model is elaborated for Mg and Zn ions, for which the thresholds are first related to a partial change of the occupancy from Li to Nb sites and second to a removal of Nb antisites due to the substitution by Mg or Zn ions. No speculation can be proposed concerning the incorporation of the newly found optical-damage-resistant ions Hf and Zr, except for the fact that by indirect evidences Hf at low concentrations incorporate onto Li sites [208, 209], whereas at high concentrations it probably occupies both cation sites [219].

At present Li-enriched (near-stoichiometric) LiNbO₃:Mg is the most intensively studied optical-damage-resistant composition [225, 226]. In these crystals the threshold Mg concentration is lower than in congruent ones in accordance with [76, 174]. In near-stoichiometric LiNbO₃:Mg the optical damage resistance occurs at [Mg] > 1–2%, that is close to the first threshold for congruent LiNbO₃:Mg. In terms of the above scenario of a two-step Mg incorporation, one may describe the first step in near-stoichiometric LiNbO₃:Mg as a complete disappearance of Nb antisites in the range ~1–2%. At a further increase of the Mg concentration the optical-damage-resistant Mg immediately starts to incorporate partially onto Nb sites. The value of the threshold Mg concentration in near-stoichiometric LiNbO₃ crystals has not been established yet. Formerly it was 2% [206], later a value of about 1% Mg was reported [225, 227], for the crystals NSLN:Mg obtained with the use of the high-temperature top-seeded solution growth method a threshold value as low as 0.67 mol.% [228] and even 0.2 mol.% Mg was observed [229]. Iyi et al. [42] assume that the threshold concentration of Mg in LiNbO₃ in the framework of the Li-vacancy

model may be taken as $2x$, where x is the Li-deficiency in the crystal. This may account for the observed scatter of the Mg threshold value in Mg-doped near-stoichiometric LiNbO₃ crystals because the degree of the near-stoichiometry strongly depends on the growth conditions and has not been specified.

Unluckily, to our knowledge no structure investigations in SLN:Mg have been performed so far, although it could clarify the origin of an extremely high optical damage resistance in these crystals.

At the end of this section, it seems appropriate to show the dependence of Li₂O and Nb₂O₅ on the MgO concentration in the congruent LiNbO₃ proposed in [211] in line with the MgO–Nb₂O₅–Li₂O phase diagram [200, 201] (Fig. 2.23). This dependence was constructed assuming an incorporation of Mg ions onto the Li sites with a simultaneous substitution for Nb_{Li} and regular Li_{Li} below the threshold and a partial incorporation of Mg onto the Nb sites above the thresholds with fulfilling the compensation conditions $[\text{Mg}_{\text{Nb}}^{3//}] - 3[\text{Mg}_{\text{Li}}^{\bullet}]$. This scheme is in a satisfactory agreement with the concentration dependencies of many properties.

In conclusion, it is worthy of repeating again that in the framework of the currently accepted defect model of LiNbO₃, the optical-damage-resistant ions, at least Mg and Zn, may be regarded as controllers of the concentration of the intrinsic defects Nb_{Li} and V_{Li}. As shown in subsequent chapters, optical, photorefractive and even ferroelectric (coercive fields) properties of optical-damage-resistant LiNbO₃ compositions are discussed in terms of a variation in the intrinsic defect structure.

2.5.2 Effect of Optical-Damage-Resistant Impurities on the Incorporation of Other Impurity Ions

The effects of Mg and Zn doping on the optical properties of LiNbO₃ crystals activated by TM or Ln³⁺ dopants are numerous reported in literature. This

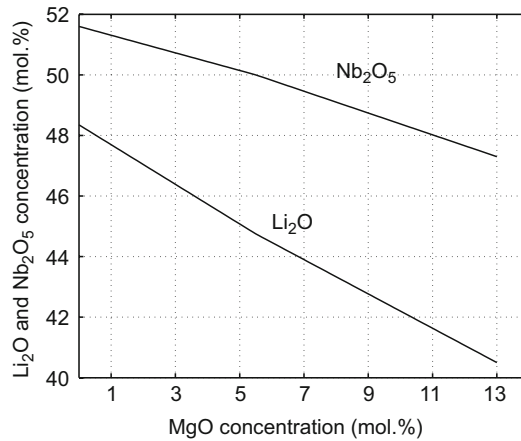


Fig. 2.23. Dependence of the Nb₂O₅ and Li₂O content in congruent Mg-doped LiNbO₃ crystals, redrawn from [211]

interest is provoked by the necessity of an insight into a microscopic origin of the optical damage resistance, and of obtaining optical-damage-resistant lasing structures on the basis of LiNbO₃:Ln³⁺. As shown in Sect. 2.4, the incorporation of TM (Fe³⁺, Cr³⁺) ions into LiNbO₃ depends on the crystal composition, namely in Li-deficient (congruent) crystals they incorporate onto the Li sites only, whereas in the near-stoichiometric crystals evidently enter partially the Nb sites. In contrast, Ln³⁺ ions seem to occupy Li sites independently of the [Li]/[Nb] ratio. Below one will see that the doping with the optical-damage-resistant ions with the above-threshold concentrations affects the lattice site of TM ions and of some Ln³⁺ ions, too. We summarize later the available results of resonance and optical studies in LiNbO₃:Mg(Zn):TM and LiNbO₃:Mg(Zn):Ln³⁺ not coming into details of the interpretation and dwelling on a qualitative description of the observed effects.

According to [174, 230, 231] Fe in Mg-doped LiNbO₃ exists in the traditional states Fe²⁺ and Fe³⁺. Figure 2.24 shows the variations in the Fe³⁺ EPR spectra in LiNbO₃:Mg:0.01%Fe and LiNbO₃:Zn:0.01%Fe crystals when increasing the Mg or Zn concentration [175] (note the identity of the curves for Mg and Zn). One may see the abrupt changes in the shapes of the spectra, particularly the appearance of an isotropic EPR-line at Mg and Zn concentrations exceeding 5.5% and 7%, respectively. Similar change of the Fe³⁺ EPR spectrum in highly doped LiNbO₃:Mg was observed in [76, 174, 231, 232]. From the parameters of the Spin–Hamiltonian in LiNbO₃:Fe:5%Mg the existence of a new axial center Fe_{Nb}³⁺ was deduced [174, 231]. Feng et al. [174] suggested that Fe_{Nb}³⁺ centers appear in the crystal after the complete substitution of Nb_{Li} by Mg. On the other hand, a detailed analysis of the dependence of the EPR spectra of Fe³⁺ on the Mg concentration in LiNbO₃:Mg:0.05%Fe [232] led to the conclusion that the spectrum of Fe_{Li}³⁺ transforms gradually within

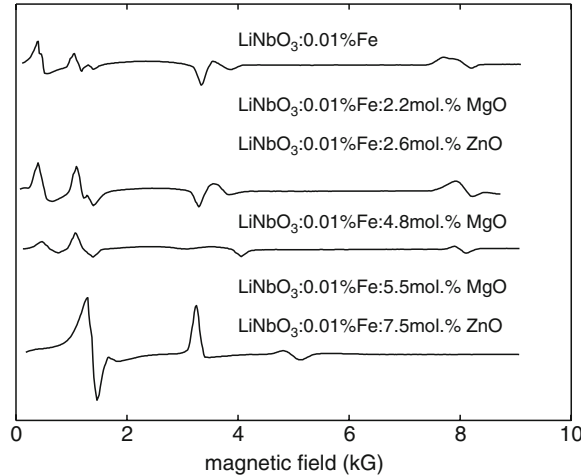


Fig. 2.24. EPR spectra of Fe-doped LiNbO₃ codoped with MgO or ZnO. The doping correspond to melt compositions, redrawn from Volk et al. [175]

a rather broad concentration range starting from $[\text{Mg}] \approx 4.6\%$. Therefore, a change of the Fe^{3+} lattice site occurs not in a step-like manner, and $\text{Fe}_{\text{Li}}^{3+}$ and $\text{Fe}_{\text{Nb}}^{3+}$ centers coexist in the concentration range 4.6–6% Mg. So, the EPR spectrum observed in a pre-threshold concentration range may be regarded as a superposition of two spectra. The change of the Fe^{3+} lattice site is of an important significance for the subsequent discussion of the microscopic origin of the optical damage resistance.

Similar variations in spectroscopic and resonance characteristics of Cr^{3+} ions at high Mg or Zn concentrations were observed, too. A sharp reconstruction of the Cr^{3+} EPR lines and the appearance of an isotropic line was detected in $\text{LiNbO}_3\text{:Cr}$ highly codoped with Mg [233–237] and Zn [237]. At low Mg or Zn concentrations the spectrum was assigned to axial $\text{Cr}_{\text{Li}}^{3+}$ centers [233,237], whereas a fundamental transformation of the spectrum at about 6% Mg was interpreted as appearance of axial $\text{Cr}_{\text{Nb}}^{3+}$ centers. Similarly to $\text{Fe}_{\text{Nb}}^{3+}$, these centers arise at a pre-threshold concentration $[\text{Mg}] > 4.6\%$ [235,236] (for $[\text{Zn}] > 4.7\%$ [237]), the ratio of $[\text{Cr}_{\text{Nb}}^{3+}]/[\text{Cr}_{\text{Li}}^{3+}]$ smoothly increasing in the range from 4.6% to 6% Mg. On the basis of EPR and ENDOR measurements Corradi et al. [238], regard this new center as a complex of $\text{Cr}_{\text{Nb}}^{3+}$ with an Mg^{2+} ion in proximity. The absorption/emission spectra in $\text{LiNbO}_3\text{:Cr}$ are also affected by high Mg or Zn doping [236,239]. The broad absorption band ${}^4\text{A}_2 \rightarrow {}^4\text{T}_1$ is shifted towards longer wavelengths, while the band ${}^4\text{A}_2 \rightarrow {}^4\text{T}_2$ is sufficiently lowered and broadened. The emission spectra in the R-line range (720–750 nm) are modified as well. The intensities of the two original R-lines are redistributed, and two new emission lines shifted towards longer wavelengths appear and are attributed to the transition ${}^4\text{A}_2 \rightarrow {}^2\text{E}$. Qualitatively, the situation is very similar to the behavior of the R-line emission in the stoichiometric $\text{LiNbO}_3\text{:Cr}$ described earlier. A new narrow p-polarized line at 781 nm is characteristic for the Cr^{3+} emission both in SLN:Cr and CLN:Cr:Mg [240]. From the correlation to the EPR data [233,238] Camarillo et al. [239] attribute the reconstruction of R-lines to the formation of Cr_{Nb} -related centers. The authors of subsequent studies in $\text{LiNbO}_3\text{:Cr:Mg}$ share this conclusion [241].

Variations of the optical absorption spectra in $\text{LiNbO}_3\text{:TM}$ under an impact of the optical-damage-resistant ions affect the appearance of the above-threshold crystals. As a result of this reconstruction of the absorption spectrum in $\text{LiNbO}_3\text{:Cr:Mg}$, the highly doped crystals transform from green to pink. In $\text{LiNbO}_3\text{:Fe:Mg(Zn)}$ with Mg(Zn) exceeding the thresholds the optical absorption at $\lambda \approx 500$ nm is sufficiently lower than in $\text{LiNbO}_3\text{:Fe}$ or low-doped $\text{LiNbO}_3\text{:Fe:Mg(Zn)}$, when compared for the same Fe concentration in the crystal. As the band at about 500 nm is related to $\text{Fe}_{\text{Li}}^{2+}$, so this observation means that at high Mg(Zn) concentrations the ratio $[\text{Fe}^{2+}]/[\text{Fe}^{3+}]$ in as-grown crystals is lesser than in $\text{LiNbO}_3\text{:Fe}$, as if the incorporation of Fe ions onto the Li sites is hampered. Consequently, the visual appearance of the above-threshold crystals is more light.

In [242] an impact of a trivalent optical-damage-resistant impurity Sc on the incorporation of Cr^{3+} ion was found. Studies by EPR and spectroscopic

methods in LiNbO₃:Cr:Sc detected the two centers Cr_{Li} and Cr_{Nb} with optical and magnetic characteristics, very similar to those of LiNbO₃:Cr:Mg(Zn).

The effects of Mg doping on the incorporation of Ti ions are of importance with regard to the formation of Ti-induced optical waveguides. In congruent crystals Ti⁴⁺ substitutes for Li [119]. To investigate its incorporation by the EPR method, the crystals have to be reduced to transform Ti⁴⁺ to the paramagnetic Ti³⁺ state [243]. EPR and optical absorption spectra in reduced LiNbO₃:Ti were attributed to Ti³⁺ centers at Li sites [244, 245], independently of the [Li]/[Nb] ratio [246]. However, high Mg doping strongly affects the Ti incorporation. Studies with EPR and optical absorption spectra in reduced LiNbO₃:Ti:6%Mg found dominant new centers interpreted as Ti³⁺ at Nb sites [246, 247], whose concentration noticeably exceeds that of Ti_{Li}³⁺.

Evidently, Mg doping affects the incorporation of the other optical-damage-resistant ion Hf. On the base of computer simulations of ion-beam channeling data it was concluded that at high Mg concentrations Hf⁴⁺ ions incorporate onto Nb sites [117, 119]. This action resembles the above mentioned evidences of the alteration of Hf lattice site in near-stoichiometric crystals [209, 219]. Here it should be mentioned that in the literature one may meet experiments on studies in LiNbO₃ doped with two types of optical-damage-resistant ions, e.g., (Zn + In) [248] or (Mg + In) [249], etc. Such combinations lead to interesting variations in physical properties, which are evidences of a nonadditivity of the effects on the defect structure. No a priori conclusion can be drawn concerning the intrinsic defect structure of these doubly doped crystals, because their incorporation onto the Li sites at low concentrations and onto both cation sites at high concentrations is concurrent. Thus one may expect a variation of the distribution coefficient of either partner depending on their concentration ratio in the melt.

As already mentioned, in the congruent LiNbO₃ several nonequivalent Ln³⁺ centers coexist on Li sites, particularly in Nd-doped crystals six ones were detected (Nd-1, Nd-2, etc.) [120]. Even at an early stage of studies in LiNbO₃:Nd:Mg the effect of a strong (about 5%) Mg codoping on the fine structure of the emission spectrum was observed (e.g., [162, 250, 251]). The authors of these works in agreement with the subsequent studies found in the emission spectrum of LiNbO₃:Nd:5%Mg two additional well separated lines in the range 875–890 nm corresponding to I(⁴I_{9/2}) → R1, R2(⁴F_{3/2}) transitions. At that time they were attributed to a perturbation of Nd_{Nb}³⁺ by the nearest Mg_{Li} [250]. In more recent works the new lines appearing in the spectra of LiNbO₃:Nd highly codoped with Mg or Zn are assigned to new centers referred to as Nd–Mg or Nd–Zn, with a very prudent assumption of their relation to Nd_{Nb} [120]. At the same time, the authors of [164] on the base of the EXAFS measurements concluded that at a high Mg concentration Nd³⁺ ions partially change their lattice sites and occupy the empty oxygen octahedra.

The influence of a high codoping with Mg or Zn was studied in LiNbO₃:Er³⁺ [252] and LiNbO₃:Yb³⁺ [253] using EPR. In crystals without codopants the EPR spectra were attributed to Er³⁺ and Yb³⁺ ions,

respectively, on the Li sites. At high Mg or Zn concentrations new EPR lines appeared, and were associated with new centers Er^{3+} (Yb^{3+}). The authors correlated these spectra with a variation of the Cr^{3+} EPR spectra in $\text{LiNbO}_3\text{:Cr:Mg}$, mentioned above and interpreted their results in terms of the location of Er^{3+} or Yb^{3+} ions at Nb sites in analogy to $\text{Cr}_{\text{Nb}}^{3+}$. Summarizing this section, one can see, that as the influence of optical-damage-resistant cations on the location of TM ions seems to be more or less understood, the situation with Ln^{3+} ions is still uncertain and requires further investigations.

2.5.3 OH-Spectra in Optical-Damage-Resistant LiNbO₃ Crystals

For an extended bibliography on this subject one may address the review [99]. The impact of optical-damage-resistant ions on the OH stretch mode characteristics present one more striking manifestation of the threshold phenomena, which are exemplified by the dependence of the IR band on the Zn concentration in $\text{LiNbO}_3\text{:Zn}$, see Fig. 2.25. Below the threshold the spectral position and the shape of the IR band is practically unchanged, above the threshold it is shifted to higher frequencies, and in a pre-threshold concentration range those bands coexist, which are characteristic for low- and heavily doped crystals. Particularly, in the pre-threshold concentration range in

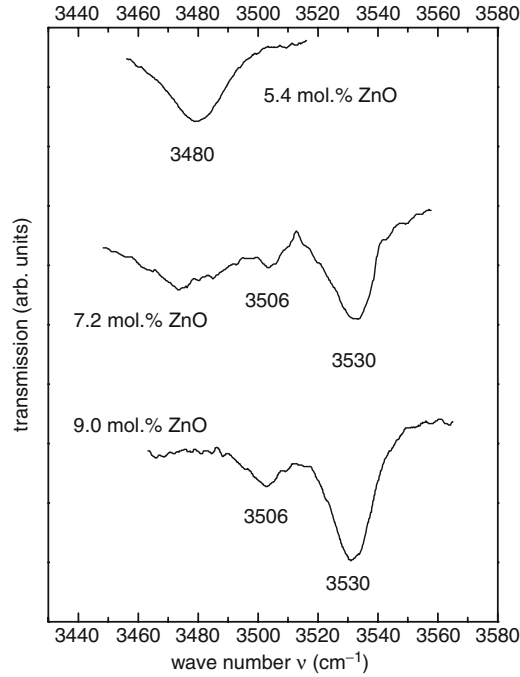


Fig. 2.25. IR transmission spectra of Zn-doped LiNbO₃ below the threshold (*top*), in the threshold region (*middle position*), and above threshold (*bottom*)

Table 2.4. Energies of the OH stretch mode in optical-damage-resistant LiNbO₃. TSSG means top seeded solution growth.

Composition/doping	Energies (cm ⁻¹)	Reference
Lithiumniobate undoped		
Congruent	3, 478, 3491	[255]
Stoichiometric	3, 466	[254, 256]
Lithiumniobate doped with damage-resistant elements		
LiNbO ₃ :Mg [Li]/[Nb] = 0.945		
<4.5% MgO	3,484	[172]
>4.5% MgO	3,534	[172]
	3,507, 3,537	[257]
LiNbO ₃ :Mg; [Li]/[Nb] = 1.1		
<3.5% MgO	3,485, 3,530, 3,540	[258], [259]
>3.5% MgO	3,540	[258], [259]
LiNbO ₃ :Mg; [Li]/[Nb] = 1.2		
<2% MgO	3,485, 3,530, 3,540	[258], [259]
>2.5% MgO	3,540	[258], [259]
LiNbO ₃ :Mg; [Li]/[Nb] = 1.38		
≈1% MgO	3,532	[226]
LiNbO ₃ :Mg; TSSG		
<1% MgO	3,466	[226]
>2% MgO	3,532	[226]
LiNbO ₃ :Zn		
<7% Zn	3,484	[260], [177]
>7% Zn	3,506, 3,535	
LiNbO ₃ :In		
>1.5%In	2,506, 3,508	[178], [249]
LiNbO ₃ :Sc		
	3,497	[261]
LiNbO ₃ :Hf [Li]/[Nb] = 0.945		
<4% HfO ₂	3,484	[262]
>4% HfO ₂	3,487	[262]
LiNbO ₃ :Zr [Li]/[Nb] = 0.945		
<2% ZrO ₂	3,484	[188]
>2% ZrO ₂	3,487	[188]

LiNbO₃:Mg and LiNbO₃:Zn the band consists of two or three peaks, whereas above the thresholds the low-frequency peak, characteristic for an undoped crystal disappears. Table 2.4 summarizes the literature data on the peak positions of the IR band in LiNbO₃ with different stoichiometry doped with the optical-damage-resistant impurities. As seen, the band-shift regularly

decreases with increasing ion valence state, being a maximum for divalent Mg or Zn and negligible for tetravalent Hf and Zr. Additionally, the presented data illustrate the repeatedly mentioned fact that the threshold concentration decreases in Li-enriched crystals. Recently, the shift of the IR band in Mg-doped near-stoichiometric crystals was observed at Mg concentrations as low as 1.5 mol.% MgO; in crystals grown by the top-seeded solution method with K₂O and even less than 1 mol.% MgO [226, 229]. No consistent microscopic model has been proposed to account for the effects of the optical-damage-resistant ions on the OH-band in LiNbO₃, although some authors try to analyze the defect structure on the base of these spectra, e.g., [207, 254].

A more complicated variation of the IR band is observed in doubly-doped crystals such as LiNbO₃:Mg, Me (Me = Nd, Cr, Ti, Mn, In, Sc) [249, 263, 264] and LiNbO₃:Zn, In [248]. In LiNbO₃:Mg, Me crystals new long-wave broadbands arise, whose intensities grow with the Me concentrations. The authors of [99] conditionally sort these crystals for two groups accordingly to the wavelengths of the new IR band. A band at about 3,507 cm⁻¹ is characteristic for Sc and In, and for TM impurities Cr and Fe. The second group includes Ln³⁺, particularly Nd in which the band appears at about 3,523 cm⁻¹. A qualitative conclusion may be drawn that the effects in doubly doped crystals are not additive, perhaps due to their concurrent incorporation onto the same lattice sites. The new bands in LiNbO₃:Mg and LiNbO₃:Mg, Me at high Mg concentrations are attributed to formation of complexes Mg-OH⁻ and Me-OH⁻-Mg.

Note that the OH-band has no practical importance, but, since its shift correlates with the occurrence of optical damage resistance, it provides a convenient tool for crystal characterization. Namely, on the basis of the position of the IR band one may conclude beforehand, whether the given impurity concentration is below or above the threshold, or, in other words, either the given composition is optical-damage-resistant or not.

Lithium Niobate

Defects, Photorefractive and Ferroelectric Switching

Volk, T.; Wöhlecke, M.

2009, XIV, 250 p. 102 illus., 2 illus. in color., Hardcover

ISBN: 978-3-540-70765-3